Oxysterols drive inflammation via GPR183 during influenza virus and SARS-CoV-2 infection

Cheng Xiang Foo[1#], Stacey Bartlett[1#], Keng Yih Chew[2,] Minh Dao Ngo[1], Helle Bielefeldt-Ohmann[2,3], Buddhika Jayakody Arachchige[4], Benjamin Matthews[4], Sarah Reed[4], Ran Wang[1], Matthew J. Sweet[3,5], Lucy Burr[6], Jane E. Sinclair[2], Rhys Parry[2], Alexander Khromykh[2,3], Kirsty R. Short[2,3], Mette Marie Rosenkilde[7] and Katharina Ronacher[1,3*]

[1]Mater Research Institute, Translational Research Institute, The University of Queensland, Brisbane, Australia
[2]School of Chemistry and Molecular Biosciences, The University of Queensland, Brisbane, Australia
[3]Australian Infectious Diseases Research Centre, The University of Queensland, Brisbane, Australia
[4]Centre for Clinical Research, The University of Queensland, Brisbane, Australia
[5]Institute for Molecular Bioscience (IMB), IMB Centre for Inflammation and Disease Research, The University of Queensland, Brisbane, Australia
[6]Department of Respiratory Medicine, Mater Adult Hospital, South Brisbane, Queensland, Australia
[7]Department of Biomedical Sciences, University of Copenhagen, Copenhagen, Denmark

[#] Contributed equally to this work.

*Correspondence:

Katharina Ronacher: Mater Research Institute, Translational Research Institute, 37 Kent Street, Brisbane 4102, QLD, Australia; email: Katharina.Ronacher@mater.uq.edu.au; phone: +61 7 3443 7633

Author Summary: Viral infections trigger oxysterol production in the lung, attracting macrophages via GPR183. Blocking GPR183 reduced inflammation and disease severity in SARS-CoV-2 infection, making GPR183 a putative target for therapeutic intervention.

Abstract

Rationale: Severe viral respiratory infections are often characterized by extensive myeloid cell infiltration and activation and persistent lung tissue injury. However, the immunological mechanisms driving excessive inflammation in the lung remain elusive.

Objectives: To identify the mechanisms that drive immune cell recruitment in the lung during viral respiratory infections and identify novel drug targets to reduce inflammation and disease severity.

Methods: Preclinical murine models of influenza virus and SARS-CoV-2 infection.

Results: Oxidized cholesterols and the oxysterol-sensing receptor GPR183 were identified as drivers of monocyte-macrophage infiltration to the lung during influenza virus (IAV) and SARS-CoV-2 infections. Both IAV and SARS-CoV-2 infections upregulated the enzymes cholesterol 25-hydroxylase (CH25H) and cytochrome P450 family 7 subfamily member B1 (CYP7B1) in the lung, resulting in local production of the oxidized cholesterols 25-hydroxycholesterol and 7α,25-dihydroxycholesterol (7α,25-OHC). Loss-of-function mutation of GPR183, or treatment with a GPR183 antagonist, reduced macrophage infiltration and inflammatory cytokine production in the lungs of IAV- or SARS-CoV-2-infected mice. The GPR183 antagonist also significantly attenuated the severity of SARS-CoV-2 infection by reducing weight loss and viral loads.

Conclusion: This study demonstrates that oxysterols drive inflammation in the lung and provides the first preclinical evidence for therapeutic benefit of targeting GPR183 during severe viral respiratory infections.

Introduction

Severe viral respiratory infections including influenza and COVID-19 are associated with extensive myeloid cell recruitment to the lung, which can lead to a cytokine storm, severe tissue injury and the development of acute respiratory distress syndrome (ARDS) (1, 2). A shift in lung macrophage composition and function is associated with COVID-19 severity. A study of >600 hospitalised patients found that in severe cases resident alveolar macrophages were depleted and replaced by large numbers of inflammatory monocytes and monocyte-derived macrophages (3). Rapid monocyte infiltration of the lung during the acute phase of severe acute respiratory coronavirus 2 (SARS-CoV-2) infection is replicated in several animal models (4-6). On the other hand, monocyte recruitment is also an essential component of repair following lung injury (7). Therapeutic approaches are required that balance pro-inflammatory and pro-repair functions of recruited monocytes.

Oxidized cholesterols, so called oxysterols, have recently emerged as markers of inflammation in the lung. Oxysterols were increased in bronchoalveolar lavage fluid (BALF) from inflamed airways after allergen challenge and strongly correlated with infiltrating leukocytes (8). They were also increased in the sputum from patients with chronic obstructive pulmonary disease (COPD) correlating with disease severity (9, 10) and in the lungs of mice after lipopolysaccharide (LPS)-induced lung inflammation (9). However, the role of oxysterols in the lung during viral respiratory infections has not been investigated.

Oxysterols have a range of properties and receptors sharing a common role in inflammation (11, 12). One of these oxysterol producing pathways leads to the production of 7α,25-hydroxycholesterol (7α,25-OHC), via cholesterol 25-hydroxylase (CH25H) and cytochrome P450 family 7 subfamily B member 1 (CYP7B1) (12, 13) (**Figure 1A**). 7α,25-OHC is the endogenous high affinity agonist of the oxidized cholesterol-sensing G protein-coupled receptor GPR183 (also known as Epstein-Barr virus-induced gene 2; EBI2) (14, 15). GPR183 is expressed on cells of the innate and adaptive immune systems, including macrophages, dendritic cells, innate lymphoid cells, eosinophils and T and B lymphocytes (8, 16-18). With its oxysterol ligands GPR183 facilitates the chemotactic distribution of immune cells to secondary lymphoid organs (12, 14, 16, 17). *In vitro* GPR183 mediates migration of human and mouse macrophages towards a 7α,25-OHC gradient (19-21).

In this study, we hypothesized that viral respiratory infections lead to the production of oxysterols in the lung and that these oxysterols contribute to excessive immune cell infiltration

89 and inflammation. We show here that oxysterols drive GPR183-dependent monocyte
90 infiltration in preclinical models of IAV and SARS-CoV-2 infection. Administration of a
91 GPR183 antagonist significantly reduces inflammation, viral load and disease severity in mice
92 infected with SARS-CoV-2. Accordingly, GPR183 is a putative host target for therapeutic
93 intervention to mitigate disease severity in viral respiratory infections.

94 **Methodology**

95 **Ethics and biosafety**

96 All experiments were approved by the University of Queensland Animal Ethics Committee
97 (MRI-UQ/596/18, AE000186) by the Institutional Biosafety Committee of the University of
98 Queensland (IBC/465B/MRI/TRI/AIBN/2021).

99 **Viral Strains**

100 Virus stocks of A/H1N1/Auckland/1/2009(H1N1) (Auckland/09) were prepared in
101 embryonated chicken eggs. Viral titers were determined by plaque assays on Madin-Darby
102 canine kidney (MDCK) cells as previously described (22). A mouse-adapted SARS-CoV-2
103 strain was obtained through serial passage of SARS-CoV-2 (B.1.351; hCoV-
104 19/Australia/QLD1520/2020, GISAID accession EPI_ISL_968081, collected on 29 December
105 2020, kindly provided by Queensland Health Forensic and Scientific Services). Six x 10^4 PFU
106 of B1.351 was administrated intranasally to ketamine-anesthetized mice. Mice were
107 monitored daily for weight loss and clinical signs of disease severity. Four days after
108 inoculation, mice were euthanized, and bronchoalveolar lavage (BAL) was performed. The
109 BALF was subsequently pooled and used to intranasally inoculate a new batch of mice. The
110 process was repeated until a virulent phenotype of the virus was observed as determined by
111 weight loss and clinical signs, which happened after four passages. To determine whether
112 the mouse adapted SARS-CoV-2 acquired mutations sequencing of viral RNA was
113 performed. Briefly, viral RNA was extracted from BALF using the Qiagen Mini kit and the
114 quality confirmed suing the Agilent Bioanalyzer with 210 Expert software. Library
115 preparations was performed using the Illumina Stranded Total RNA Ribo Zero Plus kit.
116 Sequencing was performed using the NextSeq Midoutput kit, 125bp paired-end configuration
117 with 19-25 million reads per sample. Sequencing analysis was executed using Galaxy
118 software. Whole-genome ssequencing revealed a C to T mutation in position 10804 of the
119 SARS-CoV-2 Beta genome resulting in the NSP5 mutation P252L. This mutation was rapidly
120 selected from 3.4% in the initial virus stock to 8.8% in passage one. From passage two, this

121 mutation reached consensus (60%) and underwent further fixation in passage three at 87%
122 to final frequency of 92% in passage four. A mutation in NSP5 was detected in this mouse
123 adapted SARS-CoV-2 strain (**Figure S1**). BALF of the mice from the fourth passage was
124 subsequently pooled and used to inoculate Vero E6 cells for propagation, creating the viral
125 stocks for our mouse-adapted strain. To verify the virulent phenotype of the mouse-adapted
126 virus was retained after propagation in Vero E6 cells, the cell grown virus was used to
127 inoculate a new batch of mice. The same viral stock was used to infect mice with $8x10^4$ PFU
128 for the experiments described.

129 **Bioinformatic analysis of mouse-adapted SARS-CoV-2 sequence data**

130 Base-called fastq files were mapped to the QLD1520 SARS-CoV-2 isolate (GISAID
131 accession EPI_ISL_968081) using Bowtie2 (v2.4.2) (Langmead and Salzberg 2012) under
132 default alignment conditions. Sub consensus variants of alignment files were identified using
133 iVar (v1.2.2) (Grubaugh et al. 2019) with a minimum quality score threshold of 20 and depth
134 of 5000. Coverage of mapped alignment files was determined using samtools (v1.3) depth.
135 Frequencies and coverage of variant positions were manually validated using Integrative
136 Genomics Viewer (Version: 2.7.0) (Thorvaldsdottir, Robinson, and Mesirov 2013). Variant
137 frequencies and alignment depth was 4isualized using GraphPad Prism (v9.3.1). Raw fastq
138 data generated in this study have been deposited in the Sequence Read Archive hosted by
139 the National Center for Biotechnology Information with accession number PRJNA849351.

140 **Plaque assays**

141 IAV plaque assays were carried out on confluent monolayers of MDCK cells as previously
142 described (22). SARS-CoV-2 plaque assays were carried out on Vero E6 cells as described
143 previously (23).

144 **Mouse models**

145 *Gpr183*tm1Lex were obtained from Lexicon Pharmaceuticals (The Woodlands, USA), back-
146 crossed to a C57BL/6J background and bred in-house at the Biological Resources Facility at
147 the Translational Research Institute, Australia. Eight to 10-week-old C57BL/6J and
148 *Gpr183*tm1Lex (C57BL/6J background; *Gpr183*$^{-/-}$) mice were anesthetized with isoflurane
149 (4% isoflurane, 0.4 L/min oxygen flow rate) before being inoculated intranasally with 5,500
150 PFU of A/Auckland/01/09 (H1N1). Mice were monitored for weight loss. For SARS-CoV-2
151 infection, C57BL/6J and *Gpr183*$^{-/-}$ mice were anesthetized with ketamine/Xylanzine
152 (80mg/kg/5mg/kg) before being inoculated intranasally with $8x10^4$ PFU of mouse-adapted
153 SARS-CoV-2 and monitored for weight loss. Lungs were collected at specified timepoints for

154 subsequent downstream analysis as described in supplemental data. The GPR183
155 antagonist NIBR189 (7.6 mg/kg) in 0.5% carboxymethylcellulose/0.5% Tween-80 or vehicle
156 (0.5 % carboxymethylcellulose, 0.5% Tween-80) was administrated by oral gavage from 1
157 dpi, twice daily at 12-hour intervals until the end of the experiment. IAV infected mice were
158 sacrificed at 3 dpi and 7 dpi for examination. SARS-CoV-2 infected mice were sacrificed at 2
159 dpi and 5 dpi. Lungs homogenised in DMEM for use in plaque assays and ELISAs. For RNA
160 processing, lungs were collected in TRIzol (Invitrogen). For oxysterol extraction, lungs were
161 collected in methanol. For histological analysis the lungs were fixed in 10% neutral buffered
162 formalin.

163 **RNA isolation and RT-qPCR**

164 Total RNA was isolated using ISOLATE II RNA Mini Kit (Bioline Reagents Ltd., London, UK)
165 as previously described (24). The list of primers (Sigma Aldrich) is provided in **Table S1**. The
166 relative expression (RE) of each gene using the $2^{-\Delta Ct}$ method, normalizing to the reference
167 gene (Hypoxanthine-guanine phosphoribosyltransferase; HPRT).

168 **Oxysterol extraction from lung tissues**

169 The oxysterol extraction and quantification method was adapted from Ngo et al. (24). Lung
170 lobes from IAV and SARS-CoV-2-infected mice were homogenized in methanol. Oxysterols
171 were extracted using a 1:1 dichloromethane:methanol solution containing 50 µg/mL BHT in
172 a 30°C ultrasonic bath. Tubes were flushed with nitrogen to displace oxygen, sealed with a
173 polytetrafluoroethylene (PTFE)-lined screw cap, and incubated at 30°C in the ultrasonic bath
174 for 10 mins. Following centrifugation (3,500 rpm, 5 min, 25°C), the supernatant from each
175 sample was decanted into a new tube. For liquid-liquid extraction, Dulbecco's phosphate-
176 buffered saline (DPBS) was added to the supernatant, agitated and centrifuged at 3,500 rpm
177 for 5 mins at 25°C. The organic layer was recovered and evaporated under nitrogen using a
178 27-port drying manifold (Pierce; Fisher Scientific, Fair Lawn, NJ). Oxysterols were isolated
179 by solid-phase extraction (SPE) using 200 mg, 3 mL aminopropyl SPE columns (Biotage;
180 Charlotte, NC). The samples were dissolved in 1 ml of hexane and transferred to the SPE
181 column, followed by a rinse with 1 ml of hexane to elute nonpolar compounds. Oxysterols
182 were eluted from the column with 4.5 ml of a 23:1 mixture of chloroform: methanol and dried
183 under nitrogen. Samples were resuspended in 50µl of warm (37°C) 90% methanol with 0.1%
184 DMSO, and placed in an ultrasonic bath for 5 min at 30°C. A standard curve was extracted
185 for 25-OHC (Sigma-Aldrich, H1015) and 7α,25-OHC (SML0541, Sigma-Aldrich) using the

186 above method. Dichloromethane, butylated hydroxytoluene (BHT) and hexane were
187 purchased from Sigma-Aldrich.
188
189 **Mass spectrometric quantitation of 25-OHC and 7α,25-OHC**
190 Samples were analysed on an AB Sciex QTRAP® 5500 (ABSCIEX, Redwood City, CA) mass
191 spectrometer coupled to a Shimadzu Nexera2 UHPLC. A Kinetex Pentafluorophenyl (PFP)
192 column (100 × 2.1mm, 1.7μM, 100^0A, Phenomenex) was used for the separation of 25-OHC
193 and 7α,25-OHC from other oxysterols. Mobile phase used for separation were, A - 0.1%
194 formic acid with water and B - 100% acetonitrile with 0.1% formic acid. Five μL of sample
195 were loaded at 0.5 mL/min and separated using linear gradient with increasing percentage
196 of acetonitrile. Samples were washed for 1.3 min after loading with 30% mobile phase B
197 followed by linear gradient of 30% - 70% over 9 min and 70% to 99% over 1 min. The column
198 was washed with 99% mobile phase B for 2 min followed by equilibration with 30% B 2 min
199 before next injection. Column oven and auto-sampler were operated at 50°C and 15°C,
200 respectively. Elution of analytes from the column was monitored in positive ion mode (ESI)
201 with multiple reaction monitoring on ABSciex QTRAP® mass spectrometer equipped with
202 Turbo spray ion source, which was operated at temp 550°C, ion spray voltage of 5500 V,
203 curtain gas (CUR) of 30 psi, ion source gas1 (GS1) of 65 psi and ion source gas 2 (GS2) of
204 50 psi. Quadrupole 1 and 3 were operated at unit mass resolution at all time during the
205 experiment. MRM pairs 385.3 > 367.3, 385 >133, 385.3 > 147.1 were monitored for 25-OHC
206 and for 7α,25-OHC following MRM pairs were used 383.2 > 365.3, 383.2 > 147.3, 383.2 >
207 159.0. Deuterated 25-OHC (11099, Sapphire Bioscience, Redfern, Australia) and 7α,25-OHC
208 (700078P, Merck) were used as internal standards. Following MRM transitions were recoded
209 for internal standards 391.1 > 373.2, 391.1 >133.1, 391.1>123.1 (25-OHC) and 407.2 > 389.0
210 (7α,25-OHC). De-clustering potential (DP), collision energy (CE), entrance (EP) and collision
211 cell exit potential (CXP) were optimised for each MRM pair to maximise the sensitivity. Data
212 was processed using AbSciex MultiQuant™ software (Version 3.0.3). Oxysterol
213 concentrations were subsequently normalized to the lung weights. High-performance liquid
214 chromatography (HPLC) grade methanol, acetonitrile and chloroform were purchased from
215 Merck.

216 **Cytokine quantification using ELISA**

217 Cytokines in lung homogenates were measured with DuoSet ELISA (IFNβ (DY8234-05), IFNγ
218 (DY485), IFNλ (DY1789B), IL-6 (DY406), TNFα (DY410), IL-1β (DY401), IL-10 (DY417) and
219 CCL2 (DY479), R&D systems) according to the manufacturer's protocol.

220 **Flow cytometry**

221 Lung lobes of IAV-infected mice digested in digestion buffer (Librase; Roche) and passed
222 through 40-µm nylon mesh to obtain single cell suspensions. Red blood cells lysis performed
223 using BD Pharm Lyse (BD Biosciences, San Jose, CA). Cells were labelled with: Zombie
224 Green Fixable Viability kit (423111, Biolegend), PerCP-CD45 (30-F11), Brilliant Ultraviolet
225 395-CD3e (145-2C11, BD Biosciences), Brilliant Violet (BV) 786-CD4 (L3T4, BD
226 Biosciences), PE/Cyanine7-CD11b (M1/70), BV510-CD11c (N418), APC/Cyanine7-F4/80
227 (BM8), BV605-Ly6G (1A8, BD Bioscience), PE-B220 (RA3-6B2), BV421-I-A/I-E
228 (M5/114.15.2), APC-Siglec-F (CD170, S17007L, BD bioscience) before flow cytometric
229 analysis on the BD LSRFortessa X20. Post-acquisition analysis was performed using FlowJo
230 software (TreeStar).

231 **Immunohistochemistry**

232 Heat-induced epitope retrieval was performed using citrate buffer (pH 6, 95˚C, 30 mins)
233 (BP327-1; Thermo Fisher Scientific). Sections were blocked for endogenous peroxidase
234 activity using 3% hydrogen peroxide (HL001-2.5L-P, Chem Supply, Adelaide, South
235 Australia), washed with tris-buffered saline (TBS; Bio-Rad) containing 0.05% polysorbate 20
236 (Tween-20; Sigma Aldrich; TBST) and blocked using background sniper (BS966, Biocare
237 Medical, Concord, CA) for 30 mins. Immunohistochemistry (IHC) was performed on
238 deparaffinized and rehydrated lung sections. Immunolabeling was performed with rabbit
239 antibodies against SARS-CoV-2 nucleocapsid protein antibody (1 hour at 25˚C, 1:5000)
240 (40143-R040 Sino Biological), IBA1 (2 hours at 25˚C 1:1000) (019-19741; NovaChem),
241 CH25H (4˚C overnight 1:600) (BS-6480R, Bioss Antibodies), CYP7B1 (4˚C overnight 1:1000)
242 (BS-5052R, Bioss Antibodies) and isotype control (rabbit IgG 31235, Thermo Fisher
243 Scientific) diluted in Da Vinci Green Diluent (PD900, Biocare Medical) followed by incubation
244 with horseradish peroxidase (HRP)-conjugated goat anti-rabbit Ig antibody (1:200) (ab6721,
245 Abcam). Isotype controls are shown in (**Figure S2**). Sections were washed with TBST before
246 applying chromogen detection, using diaminobenzidine (ab64238, DAB substrate kit Abcam,)
247 as per the manufacturer's instructions. Counterstaining was performed with Mayer's
248 hematoxylin (Sigma-Aldrich) before dehydrating the sections in a series of increasing ethanol

concentrations (70% to 100% ethanol). Sections were clarified with xylene, and mounted using a xylene-based mounting medium (15-184-40, SHURMount Mounting Media, Fisher scientific). Slides were scanned in an Olympus SLIDEVIEW VS200 using a 20x objective. DAB-positive areas were quantified using ImageJ (https://imagej.nih.gov/ij/).

Statistical analysis

Data were analysed on GraphPad Prism software. Data were also assessed for normality using Shapiro-Wilk test. Spearman rank correlation was used to analyse correlations. For two group comparisons, parametric Student's two-tailed t test was used for normally distributed data while nonparametric Mann-Whitney U test was used for skewed data that deviate from normality.

Results

IAV infection increases CH25H and CYP7B1 expression and oxysterol production in the lung

To investigate whether IAV infection induces the production of oxidized cholesterols, we infected mice with IAV (**Figure 1B**) and determined the mRNA expression of oxysterol producing enzymes in the lung. *Ch25h* and *Cyp7b1* mRNA was increased in the lungs of IAV-infected mice compared to uninfected animals (**Figure 1C**). Similarly, CH25H and CYP7B1 protein expression was also increased, as demonstrated by immunohistochemical labelling of lung sections with antibodies detecting CH25H and CYP7B1 protein (**Figure 1D,E**). The induction of oxysterol producing enzymes was associated with increased concentrations of the oxysterols 7α,25-OHC and 25-OHC in IAV-infected lungs at both 3 days post infection (dpi) and 7 dpi (**Figure 1F, G**). In uninfected lungs, 7α,25-OHC was undetectable in most samples tested. Consistent with the increase in oxysterols, *Gpr183* mRNA was increased at 3 dpi and 7 dpi (**Figure S3A**), suggesting increased recruitment of GPR183-expressing immune cells to the lung upon infection. *Gpr183* expression was positively correlated with *Ch25h* and *Cyp7b1* (**Figure S3B, C**).

Gpr183$^{-/-}$ mice have reduced macrophage infiltration into the lungs upon IAV infection

To investigate whether oxysterol-mediated immune cell recruitment is dependent on oxysterol-sensing GPR183, we performed experiments in mice genetically deficient in

280 *Gpr183* (*Gpr183*$^{-/-}$). *Gpr183*$^{-/-}$ mice are viable and exhibit normal gross phenotype (25).
281 However, upon infection with IAV, *Gpr183*$^{-/-}$ mice had lower IBA1^{+} macrophage numbers in
282 the lung at 3 dpi and 7 dpi compared to infected C57BL/6J controls (**Figure 2A**). *Gpr183*
283 expression was positively correlated with mRNA expression of the pro-inflammatory
284 cytokines *Il6, Tnf* and *Ccl2* in C57BL/6J mice (**Figure S4**) and reduced macrophage
285 infiltration in *Gpr183*$^{-/-}$ mice was associated with reduced *Il6* and *Tnf,* but not *Ccl2* at 7 dpi
286 (**Figure S5**). Body weights and viral titers through the course of IAV infection were
287 comparable across the two genotypes (**Figure S6**). These results demonstrate that GPR183
288 is required for macrophage infiltration into the lung upon IAV infection and that lower
289 macrophage numbers are associated with reduced expression of pro-inflammatory cytokines.

290 **GPR183 inhibition reduces macrophage infiltration**

291 To investigate whether GPR183 is a putative therapeutic target to reduce inflammation, the
292 synthetic GPR183 antagonist NIBR189 (14, 21) was administered to C57BL/6J mice twice
293 daily starting from 24 h post-infection until the end of the experiment (**Figure 2B**). Like
294 *Gpr183*$^{-/-}$ mice, C57BL/6J animals treated with NIBR189 had significantly reduced
295 macrophage infiltration into the lung both at 3 and 7 dpi as determined by IHC (**Figure 2C**).

296 In addition, flow cytometry analysis was performed on lung single cell suspensions from
297 C57BL/6J and *Gpr183*$^{-/-}$ mice treated with NIBR189 and vehicle, respectively, using a
298 previously published gating strategy (26) (**Figure S7**). NIBR189-treated C57BL/6J mice and
299 *Gpr183*$^{-/-}$ mice had lower percentages of macrophages (F480^{high}/CD11b^{+}/Ly6G^{-}/SigF^{-})
300 (**Figure 3A, B**) compared to vehicle-treated C57BL/6J animals after IAV infection. NIBR189
301 treatment did not change the percentages of other immune cell subsets in the lung, including
302 neutrophils (B220^{-}/CD3^{-}/Ly6G^{+}/CD11b^{+}) (**Figure 3A, C**), CD4+ T cells, CD8+ T cells, B cells,
303 DCs, and alveolar macrophages (**Figure S8**). Body weights and lung viral loads were not
304 affected by genotype or treatment (**Figure S9**).

305 Taken together our results demonstrate that the GPR183 antagonist NIBR189 significantly
306 reduced the infiltration of macrophages to the lung without affecting the recruitment of other
307 immune cell subsets to the site of infection.

308 **GPR183 inhibition reduces IAV-induced pro-inflammatory cytokine concentrations**

309 We next determined if the reduced macrophage infiltration mediated by the GPR183
310 antagonist NIBR189 results in reduced inflammatory cytokine production in the lung. At 3 dpi,
311 no significant differences in cytokine production were observed between treatment groups

312 (**Figure S10**). However, IAV-Infected C57BL/6J mice treated with NIBR189 had significantly
313 lower concentrations of IL-6, TNF and IFNβ (**Figure 4A-D**) at 7 dpi. This was again
314 comparable to the phenotype of IAV-infected *Gpr183*$^{-/-}$ mice, with NIBR189 treatment having
315 no additional effect in mice deficient in GPR183. In addition, no significant differences were
316 observed in IFNλ across the two timepoints (**Figure 4D and Figure S10**) demonstrating that
317 the GPR183 antagonist treatment does not negatively impact the production of type III IFNs
318 which are important for viral control in the lung (27). No differences between treatment groups
319 were observed at either timepoint for protein concentrations of IL-1β, CCL2 or IFNγ between
320 treatment groups (**Figure S10 and S11**). Thus, GPR183 can be inhibited pharmacologically
321 to reduce proinflammatory cytokines upon severe IAV infection.

322 **GPR183 inhibition reduces SARS-CoV-2 infection severity**

323 Excessive macrophage infiltration and activation is a hallmark of severe COVID-19 (3, 28).
324 To evaluate whether the benefits of inhibiting GPR183 extend to SARS-CoV-2 infection, we
325 established a mouse-adapted SARS-CoV-2 strain by passaging the Beta variant of SARS-
326 CoV-2 (B.1.351) four times in C57BL/6J mice. This resulted in a viral stock that contained a
327 mutation in NSP5 and caused clinical signs in infected mice as indicated by body weight loss
328 (**Figure S1**). Consistent with the IAV infection results, mRNA expression of *Ch25h* and
329 *Cyp7b1* was significantly upregulated in the lungs of SARS-CoV-2 infected mice compared
330 to uninfected mice (**Figure 5A**). This was confirmed also at the protein level by IHC (**Figure**
331 **5B, C**). Further, 25-OHC and 7α,25-OHC concentrations in lung homogenates were
332 significantly increased at 2 dpi, returning to uninfected levels by 5 dpi by which time the
333 animals began to recover from the infection (**Figure 5D**). NIBR189 or vehicle was
334 administered to C57BL/6J or *Gpr183*$^{-/-}$ mice twice daily from 24 h post-SARS-CoV-2 infection
335 until the end of the experiment (**Figure 6A**). NIBR189-treated C57BL/6J mice lost significantly
336 less weight and recovered faster compared to infected C57BL/6J mice receiving vehicle
337 (**Figure 6B and S12**). Similarly, *Gpr183*$^{-/-}$ had less severe SARS-CoV-2 infection.
338 Collectively, these data demonstrate that oxysterols are produced in the lung upon SARS-
339 CoV-2 infection and inhibition of GPR183 significantly reduced the severity of SARS-CoV-2
340 infection.

341 **GPR183 inhibition reduces macrophage infiltration and inflammatory cytokine**
342 **expression in the lung of SARS-CoV-2 infected mice**

343 Next, we investigated whether the inhibition of GPR183 also decreases macrophage
344 infiltration and inflammatory cytokines in the lung. SARS-CoV-2-infected C57BL/6J mice

345 treated with NIBR189 had significantly reduced macrophage infiltration into the lung at 2 dpi
346 and 5 dpi (**Figure 6C**). NIBR189 treatment was also associated with reduced *Tnf, Il10* and
347 *Ifng* mRNA expression at 2 dpi (**Figure 7A-C**), as well as reduced *Tnf*, *Il1b and Il6* expression
348 at 5 dpi (**Figure 7D-F**). Early interferon responses were not affected by NIBR189 treatment
349 with comparable *Ifnb* and *Ifnl* expression at 2 dpi in C57BL/6J mice that received NIBR189
350 treatment versus vehicle (**Figure 8A, B**). Late interferon responses (5 dpi) were significantly
351 lower in NIBR-treated animals compared to controls (**Figure 8C, D**). No differences between
352 treatment groups were observed for mRNAs encoding *Ccl2, Il1b*, or *Il6* at 2 dpi as well as
353 those encoding *Ccl2*, *Il10* and *Ifng* at 5 dpi (**Figure S13**). These results demonstrate that
354 reduced macrophage infiltration in NIBR-treated mice was associated with reduced pro-
355 inflammatory cytokine expression in the lung, while the early antiviral IFN responses
356 remained unchanged. The mechanism(s) by which oxysterols attract macrophages to the
357 lung to produce pro-inflammatory cytokines are therefore conserved across viral infections.

358 **GPR183 inhibition reduces SARS-CoV-2 loads**

359 Finally, we investigated whether the reduced macrophage infiltration and inflammatory
360 cytokine profile in the lung of the NIBR189-treated mice is associated with altered viral loads.
361 Viral nucleocapsid protein (Np) expression was reduced in C57BL/6J mice treated with
362 NIBR189 compared to those administered vehicle at 2 dpi (**Figure 9A, B**). Np expression
363 was not detected at 5 dpi, when the animals recovered from the infection. However, at the
364 mRNA level, viral *Mpro* RNA loads in the lungs of NIBR189-treated mice were significantly
365 lower at 5 dpi (**Figure 9C**). In summary, we demonstrate here that GPR183 inhibition reduces
366 viral loads, macrophage infiltration and production of pro-inflammatory cytokines that are
367 typically associated with immunopathology in the lung (**Figure 10**).

368 **Discussion**

369 Here, we report that the oxysterols 25-OHC and 7α,25-OHC are produced in the lung upon
370 infection with either IAV or SARS-CoV-2 and attract monocytes-macrophages in a GPR183
371 dependent manner to the lung. Excessive macrophage infiltration and inflammation triggers
372 lung pathology and results in severe respiratory infection outcomes (1, 2, 29). Reduced
373 macrophage infiltration in *Gpr183*$^{-/-}$ mice, as well as in C57BL/6J mice treated with the
374 GPR183 antagonist NIBR189, was associated with reduced inflammatory cytokine
375 production in the lungs of IAV and SARS-CoV-2 infected animals. Blocking GPR183 in
376 SARS-CoV-2-infected mice significantly improved SARS-CoV-2 infection severity and
377 attenuated viral loads. The antagonist had no impact on IAV viral loads and whether this is
378 due to pathogen-specific effects or due to more severe disease observed by increased weight
379 loss in the IAV model compared to the SARS-CoV-2 model, remains to be investigated.
380 However, macrophage infiltration and cytokine production was reduced in both viral models.

381 In non-human primates, influenza virus infection leads to infiltration of myeloid cells into the
382 lungs (30). Similarly, in several animal models of acute infection with SARS-CoV-2,
383 macrophages rapidly infiltrate the lungs (4-6). Patients with severe COVID-19 infection had
384 higher proportions of macrophages and neutrophils in BALF, with the macrophage phenotype
385 from deceased COVID-19 patients being more activated (28). This strongly implicates
386 macrophages as key cellular contributors to COVID-19-associated hyperinflammation. In
387 BALF from patients with severe COVID-19, the chemokines CCL2 and CCL7 that recruit
388 monocytes to the lung via the chemokine receptor CCR2 are also significantly enriched (31).
389 Historically, chemokines have been considered as the main drivers of immune cell migration
390 into the lung; however, our work here reveals that oxysterols have a non-redundant role in
391 macrophage infiltration. Similar to our observations in *Gpr183*$^{-/-}$ mice, mice lacking the
392 chemokine receptor CCR2 have a significant delay in macrophage infiltration into the lung
393 (26). However, CCR2 is also required for T cell migration, therefore, animals lacking CCR2
394 also had delayed T cell infiltration, which correlated with significantly higher pulmonary viral
395 titers (32). Although GPR183 is expressed on T cells it is not essential for T cell migration
396 into the lung (33) and thus blocking GPR183 in our preclinical models did not negatively
397 impact the T cell compartment nor other immune cell subsets.

398 We recently showed in a murine model of *Mycobacterium tuberculosis* (Mtb) infection that
399 both GPR183 and CYP7B1, which produces the endogenous high affinity GPR183 agonist
400 7α,25-OHC, are required for rapid macrophage infiltration into the lung upon bacterial

401 infection (24). In the Mtb model, GPR183 was also required for infiltration of eosinophils into
402 the lung (18).

403 Reduced macrophage infiltration in both *Gpr183*$^{-/-}$ mice and C57BL/6J mice treated with the
404 GPR183 antagonist NIBR189 was associated with reduced pro-inflammatory cytokine
405 production in the lung of both IAV and SARS-CoV-2 infected animals, likely due to lower
406 numbers of pro-inflammatory macrophages present in the tissue. However, we cannot
407 exclude a direct effect of the GPR183 antagonist on cytokine production in macrophages and
408 potentially other immune cell subsets like T cells. We previously showed that GPR183 is a
409 constitutively negative regulator of type I IFNs in primary human monocytes infected with Mtb
410 (34). *In vitro* activation of GPR183 with the agonist 7α,25-OHC reduced Mtb-induced *Ifnb*
411 mRNA levels, while the GPR183 antagonist GSK682753 significantly increased *Ifnb* mRNA
412 expression elicited by Mtb (34). This antagonist did not affect *Tnf* transcription in these *in vitro*
413 assays; however, it cannot be excluded that NIBR189 used in the experiments presented
414 here directly affects cytokine expression in macrophages or other immune cell subsets.

415 Irrespective of the exact mechanism, reduced pro-inflammatory cytokine production was
416 associated with reduced SARS-CoV-2 infection severity. Excessive production of
417 proinflammatory cytokines contributes to the immunopathology in COVID-19 patients with
418 severe disease (35). Therefore, lower pro-inflammatory cytokine production in animals
419 treated with NIBR189 can explain, at least in part, the better disease outcomes compared to
420 vehicle-treated animals. While cytokines can be detrimental to the host and contribute to the
421 development of cytokine storms (36), early type I and III IFNs are crucial in controlling viral
422 replication during IAV (37, 38) and SARS-CoV-2 infections (39, 40), whereas prolonged type
423 I IFN responses can be detrimental to the host (41). The GPR183 antagonist did not alter
424 early type I or III IFN responses in SARS-CoV-2-infected animals, suggesting that the anti-
425 viral response was not impaired by the treatment. However, antagonising GPR183 prevented
426 a prolonged IFN response, which was associated with more effective viral clearance
427 observed in NIBR189-treated animals.

428 While several oxysterols can have a direct anti-viral effect (12), it is not known whether
429 NIBR189 directly affects viral entry or replication. CH25H/25-OHC have been shown to inhibit
430 SARS-CoV-2 infection *in vitro* by blocking the virus-host cell membrane fusion (42, 43). It is
431 unlikely that NIBR189 directly affects viral entry and/or replication, given that it is structurally

432 very different from cholesterols and probably not able to disrupt the host cell membrane
433 composition typical for other anti-viral oxysterols.

434 We propose that GPR183, which belongs to the GPCR family, is a novel drug target for
435 severe COVID-19. GPCRs are popular targets because of their pharmacological tractability.
436 Indeed, 34% of all FDA approved drugs are directed against members of this receptor family,
437 with this accounting for global sales volumes of over 180 billion US dollars (44). In our SARS-
438 CoV-2 model the GPR183 antagonist demonstrated a dual benefit by not only reducing pro-
439 inflammatory cytokines without compromising early type I and type III IFN responses, but
440 also by reducing viral loads. Other immunosuppressive therapies used in severe COVID-19
441 like glucocorticoids can increase ACE2 expression which promotes viral entry and replication
442 (45, 46). Consistent with this, glucocorticoid use delays SARS-CoV-2 clearance (47).
443 Glucocorticoids can also affect antibody production. While it remains to be established
444 whether NIBR189 has a similar effect, short term use of a GPR183 antagonist during the
445 acute viral infection is unlikely to negatively impact antibody responses. Currently available
446 antiviral treatments are effective, but mutations in SARS-CoV-2 conferring resistance to new
447 antivirals are already emerging (48). Therefore, adjunct host-directed therapy with a GPR183
448 antagonist together with conventional antivirals may increase treatment efficacy. Since a
449 GPR183 antagonist targets the host and not the virus it is not anticipated that viruses will
450 develop resistance against host directed therapy (49). Further, a GPR183 antagonist-based
451 therapy can also be immediately effective against newly emerging SARS-CoV-2 variants
452 without further adaption.

453 In summary, we provide the first preclinical evidence of GPR183 as a novel host target for
454 therapeutic intervention to reduce macrophage-mediated hyperinflammation, SARS-CoV-2
455 loads and disease severity in COVID-19.

Acknowledgements

This study was supported by grants to KR from the Mater Foundation, the Australian Respiratory Council, Diabetes Australia, and the Australian Infectious Diseases Research Centre. SB was supported by an early career seed grant from the Mater Foundation. The Translational Research Institute is supported by a grant from the Australian Government. We thank A/Prof Sumaira Hasnain for sharing antibodies used in this study. We thank the Queensland Health Forensic and Scientific Services, Queensland Department of Health, for providing SARS-CoV-2 isolate. We acknowledge the technical assistance of the team that operates and maintains the Australian Galaxy service (https://usegalaxy.org.au/). The Danish Council for Independent Research I Medical Sciences supported MMR. MJS is supported by a National Health and Medical Research Council of Australia Investigator grant (APP1194406). KRS is funded by the NHMRC Investigator Grant (2007919) and is consultant for Sanofi, Roche and NovoNordisk. MMR is co-founder of Antag Therapeutics and of Synklino. The opinions and data presented in this manuscript are of the authors and are independent of these relationships. Other authors declare no competing interests. We thank Profs David Hume, Jean-Pierre Levesque and Maher Gandhi for critical review of the manuscript.

Author contributions

Conceptualization: CXF, SB, MJS, KRS, MMR, KR Methodology: KYC, HBO, BJA, BM,SR Investigation: CXF, SB, KYC, MDN, HBO, BJA, BM, SR, RW, LB, JES, RP, AK Writing-original draft: CXF, SB, KR Writing-review and editing: all authors. Funding acquisition: SB, KRS, MMR, KR.

485 **References**

486 1. Flerlage T, Boyd DF, Meliopoulos V, Thomas PG, Schultz-Cherry S. 2021. Influenza
487 virus and SARS-CoV-2: pathogenesis and host responses in the respiratory tract. Nat
488 Rev Microbiol 19:425-441.
489 2. Short KR, Kroeze E, Fouchier RAM, Kuiken T. 2014. Pathogenesis of influenza-
490 induced acute respiratory distress syndrome. Lancet Infect Dis 14:57-69.
491 3. Chen ST, Park MD, Del Valle DM, Buckup M, Tabachnikova A, Simons NW, Mouskas
492 K, Lee B, Geanon D, D'Souza D, Dawson T, Marvin R, Nie K, Thompson RC, Zhao Z,
493 LeBerichel J, Chang C, Jamal H, Chaddha U, Mathews K, Acquah S, Brown SA, Reiss
494 M, Harkin T, Feldmann M, Powell CA, Hook JL, Kim-Schulze S, Rahman AH, Brown
495 BD, Mount Sinai C-BT, Beckmann ND, Gnjatic S, Kenigsberg E, Charney AW, Merad
496 M. 2022. Shift of lung macrophage composition is associated with COVID-19 disease
497 severity and recovery. bioRxiv doi:10.1101/2022.01.11.475918.
498 4. Speranza E, Williamson BN, Feldmann F, Sturdevant GL, Perez-Perez L, Meade-
499 White K, Smith BJ, Lovaglio J, Martens C, Munster VJ, Okumura A, Shaia C,
500 Feldmann H, Best SM, de Wit E. 2021. Single-cell RNA sequencing reveals SARS-
501 CoV-2 infection dynamics in lungs of African green monkeys. Sci Transl Med 13.
502 5. Lee JS, Koh JY, Yi K, Kim YI, Park SJ, Kim EH, Kim SM, Park SH, Ju YS, Choi YK,
503 Park SH. 2021. Single-cell transcriptome of bronchoalveolar lavage fluid reveals
504 sequential change of macrophages during SARS-CoV-2 infection in ferrets. Nat
505 Commun 12:4567.
506 6. Singh DK, Aladyeva E, Das S, Singh B, Esaulova E, Swain A, Ahmed M, Cole J,
507 Moodley C, Mehra S, Schlesinger LS, Artyomov MN, Khader SA, Kaushal D. 2022.
508 Myeloid cell interferon responses correlate with clearance of SARS-CoV-2. Nat
509 Commun 13:679.
510 7. Mirchandani AS, Jenkins SJ, Bain CC, Sanchez-Garcia MA, Lawson H, Coelho P,
511 Murphy F, Griffith DM, Zhang A, Morrison T, Ly T, Arienti S, Sadiku P, Watts ER,
512 Dickinson RS, Reyes L, Cooper G, Clark S, Lewis D, Kelly V, Spanos C, Musgrave
513 KM, Delaney L, Harper I, Scott J, Parkinson NJ, Rostron AJ, Baillie JK, Clohisey S,
514 Pridans C, Campana L, Lewis PS, Simpson AJ, Dockrell DH, Schwarze J, Hirani N,
515 Ratcliffe PJ, Pugh CW, Kranc K, Forbes SJ, Whyte MKB, Walmsley SR. 2022. Hypoxia
516 shapes the immune landscape in lung injury and promotes the persistence of
517 inflammation. Nat Immunol 23:927-939.
518 8. Shen ZJ, Hu J, Kashi VP, Kelly EA, Denlinger LC, Lutchman K, McDonald JG, Jarjour
519 NN, Malter JS. 2017. Epstein-Barr Virus-induced Gene 2 Mediates Allergen-induced
520 Leukocyte Migration into Airways. Am J Respir Crit Care Med 195:1576-1585.
521 9. Jia J, Conlon TM, Sarker RS, Tasdemir D, Smirnova NF, Srivastava B, Verleden SE,
522 Gunes G, Wu X, Prehn C, Gao J, Heinzelmann K, Lintelmann J, Irmler M, Pfeiffer S,
523 Schloter M, Zimmermann R, Hrabe de Angelis M, Beckers J, Adamski J, Bayram H,
524 Eickelberg O, Yildirim AO. 2018. Cholesterol metabolism promotes B-cell positioning
525 during immune pathogenesis of chronic obstructive pulmonary disease. EMBO Mol
526 Med 10.
527 10. Sugiura H, Koarai A, Ichikawa T, Minakata Y, Matsunaga K, Hirano T, Akamatsu K,
528 Yanagisawa S, Furusawa M, Uno Y, Yamasaki M, Satomi Y, Ichinose M. 2012.
529 Increased 25-hydroxycholesterol concentrations in the lungs of patients with chronic
530 obstructive pulmonary disease. Respirology 17:533-40.
531 11. Reinmuth L, Hsiao CC, Hamann J, Rosenkilde M, Mackrill J. 2021. Multiple Targets
532 for Oxysterols in Their Regulation of the Immune System. Cells 10.

533 12. Foo CX, Bartlett S, Ronacher K. 2022. Oxysterols in the Immune Response to
534 Bacterial and Viral Infections. Cells 11.
535 13. Mutemberezi V, Guillemot-Legris O, Muccioli GG. 2016. Oxysterols: From cholesterol
536 metabolites to key mediators. Prog Lipid Res 64:152-169.
537 14. Hannedouche S, Zhang J, Yi T, Shen W, Nguyen D, Pereira JP, Guerini D,
538 Baumgarten BU, Roggo S, Wen B, Knochenmuss R, Noel S, Gessier F, Kelly LM,
539 Vanek M, Laurent S, Preuss I, Miault C, Christen I, Karuna R, Li W, Koo DI, Suply T,
540 Schmedt C, Peters EC, Falchetto R, Katopodis A, Spanka C, Roy MO, Detheux M,
541 Chen YA, Schultz PG, Cho CY, Seuwen K, Cyster JG, Sailer AW. 2011. Oxysterols
542 direct immune cell migration via EBI2. Nature 475:524-7.
543 15. Liu C, Yang XV, Wu J, Kuei C, Mani NS, Zhang L, Yu J, Sutton SW, Qin N, Banie H,
544 Karlsson L, Sun S, Lovenberg TW. 2011. Oxysterols direct B-cell migration through
545 EBI2. Nature 475:519-23.
546 16. Spann NJ, Glass CK. 2013. Sterols and oxysterols in immune cell function. Nat
547 Immunol 14:893-900.
548 17. Emgard J, Kammoun H, Garcia-Cassani B, Chesne J, Parigi SM, Jacob JM, Cheng
549 HW, Evren E, Das S, Czarnewski P, Sleiers N, Melo-Gonzalez F, Kvedaraite E,
550 Svensson M, Scandella E, Hepworth MR, Huber S, Ludewig B, Peduto L, Villablanca
551 EJ, Veiga-Fernandes H, Pereira JP, Flavell RA, Willinger T. 2018. Oxysterol Sensing
552 through the Receptor GPR183 Promotes the Lymphoid-Tissue-Inducing Function of
553 Innate Lymphoid Cells and Colonic Inflammation. Immunity 48:120-132 e8.
554 18. Bohrer AC, Castro E, Tocheny CE, Assmann M, Schwarz B, Bohrnsen E, Makiya MA,
555 Legrand F, Hilligan KL, Baker PJ, Torres-Juarez F, Hu Z, Ma H, Wang L, Niu L, Zilu
556 W, Lee SH, Kamenyeva O, Program TI, Kauffman KD, Donato M, Sher A, Barber DL,
557 Via LE, Scriba TJ, Khatri P, Song Y, Wong K-W, Bosio CM, Klion AD, Mayer-Barber
558 KD. 2022. Rapid GPR183-mediated recruitment of eosinophils to the lung after
559 Mycobacterium tuberculosis infection. doi:10.1101/2022.02.18.480919
560 %J bioRxiv:2022.02.18.480919.
561 19. Rutkowska A, O'Sullivan SA, Christen I, Zhang J, Sailer AW, Dev KK. 2016. The EBI2
562 signalling pathway plays a role in cellular crosstalk between astrocytes and
563 macrophages. Sci Rep 6:25520.
564 20. Preuss I, Ludwig MG, Baumgarten B, Bassilana F, Gessier F, Seuwen K, Sailer AW.
565 2014. Transcriptional regulation and functional characterization of the oxysterol/EBI2
566 system in primary human macrophages. Biochem Biophys Res Commun 446:663-8.
567 21. Gessier F, Preuss I, Yin H, Rosenkilde MM, Laurent S, Endres R, Chen YA, Marsilje
568 TH, Seuwen K, Nguyen DG, Sailer AW. 2014. Identification and characterization of
569 small molecule modulators of the Epstein-Barr virus-induced gene 2 (EBI2) receptor.
570 J Med Chem 57:3358-68.
571 22. Short KR, Diavatopoulos DA, Reading PC, Brown LE, Rogers KL, Strugnell RA,
572 Wijburg OL. 2011. Using bioluminescent imaging to investigate synergism between
573 Streptococcus pneumoniae and influenza A virus in infant mice. J Vis Exp
574 doi:10.3791/2357.
575 23. Schimmel L, Chew KY, Stocks CJ, Yordanov TE, Essebier P, Kulasinghe A, Monkman
576 J, Dos Santos Miggiolaro AFR, Cooper C, de Noronha L, Schroder K, Lagendijk AK,
577 Labzin LI, Short KR, Gordon EJ. 2021. Endothelial cells are not productively infected
578 by SARS-CoV-2. Clin Transl Immunology 10:e1350.
579 24. Ngo MD, Bartlett S, Bielefeldt-Ohmann H, Foo CX, Sinha R, Arachige BJ, Reed S,
580 Mandrup-Poulsen T, Rosenkilde MM, Ronacher K. 2022. A blunted GPR183/oxysterol
581 axis during dysglycemia results in delayed recruitment of macrophages to the lung
582 during M. tuberculosis infection. J Infect Dis doi:10.1093/infdis/jiac102.

583 25. Pereira JP, Kelly LM, Xu Y, Cyster JG. 2009. EBI2 mediates B cell segregation
584 between the outer and centre follicle. Nature 460:1122-6.
585 26. Poczobutt JM, Gijon M, Amin J, Hanson D, Li H, Walker D, Weiser-Evans M, Lu X,
586 Murphy RC, Nemenoff RA. 2013. Eicosanoid profiling in an orthotopic model of lung
587 cancer progression by mass spectrometry demonstrates selective production of
588 leukotrienes by inflammatory cells of the microenvironment. PLoS One 8:e79633.
589 27. Zhou JH, Wang YN, Chang QY, Ma P, Hu Y, Cao X. 2018. Type III Interferons in Viral
590 Infection and Antiviral Immunity. Cell Physiol Biochem 51:173-185.
591 28. Liao M, Liu Y, Yuan J, Wen Y, Xu G, Zhao J, Cheng L, Li J, Wang X, Wang F, Liu L,
592 Amit I, Zhang S, Zhang Z. 2020. Single-cell landscape of bronchoalveolar immune
593 cells in patients with COVID-19. Nat Med 26:842-844.
594 29. Baskin CR, Bielefeldt-Ohmann H, Tumpey TM, Sabourin PJ, Long JP, Garcia-Sastre
595 A, Tolnay AE, Albrecht R, Pyles JA, Olson PH, Aicher LD, Rosenzweig ER, Murali-
596 Krishna K, Clark EA, Kotur MS, Fornek JL, Proll S, Palermo RE, Sabourin CL, Katze
597 MG. 2009. Early and sustained innate immune response defines pathology and death
598 in nonhuman primates infected by highly pathogenic influenza virus. Proc Natl Acad
599 Sci U S A 106:3455-60.
600 30. Corry J, Kettenburg G, Upadhyay AA, Wallace M, Marti MM, Wonderlich ER, Bissel
601 SJ, Goss K, Sturgeon TJ, Watkins SC, Reed DS, Bosinger SE, Barratt-Boyes SM.
602 2022. Infiltration of inflammatory macrophages and neutrophils and widespread
603 pyroptosis in lung drive influenza lethality in nonhuman primates. PLoS Pathog
604 18:e1010395.
605 31. Zhou Z, Ren L, Zhang L, Zhong J, Xiao Y, Jia Z, Guo L, Yang J, Wang C, Jiang S,
606 Yang D, Zhang G, Li H, Chen F, Xu Y, Chen M, Gao Z, Yang J, Dong J, Liu B, Zhang
607 X, Wang W, He K, Jin Q, Li M, Wang J. 2020. Heightened Innate Immune Responses
608 in the Respiratory Tract of COVID-19 Patients. Cell Host Microbe 27:883-890 e2.
609 32. Dawson TC, Beck MA, Kuziel WA, Henderson F, Maeda N. 2000. Contrasting effects
610 of CCR5 and CCR2 deficiency in the pulmonary inflammatory response to influenza A
611 virus. Am J Pathol 156:1951-9.
612 33. Hoft SG, Sallin MA, Kauffman KD, Sakai S, Ganusov VV, Barber DL. 2019. The Rate
613 of CD4 T Cell Entry into the Lungs during Mycobacterium tuberculosis Infection Is
614 Determined by Partial and Opposing Effects of Multiple Chemokine Receptors. Infect
615 Immun 87.
616 34. Bartlett S, Gemiarto AT, Ngo MD, Sajiir H, Hailu S, Sinha R, Foo CX, Kleynhans L,
617 Tshivhula H, Webber T, Bielefeldt-Ohmann H, West NP, Hiemstra AM, MacDonald
618 CE, Christensen LVV, Schlesinger LS, Walzl G, Rosenkilde MM, Mandrup-Poulsen T,
619 Ronacher K. 2020. GPR183 Regulates Interferons, Autophagy, and Bacterial Growth
620 During Mycobacterium tuberculosis Infection and Is Associated With TB Disease
621 Severity. Front Immunol 11:601534.
622 35. Del Valle DM, Kim-Schulze S, Huang HH, Beckmann ND, Nirenberg S, Wang B, Lavin
623 Y, Swartz TH, Madduri D, Stock A, Marron TU, Xie H, Patel M, Tuballes K, Van
624 Oekelen O, Rahman A, Kovatch P, Aberg JA, Schadt E, Jagannath S, Mazumdar M,
625 Charney AW, Firpo-Betancourt A, Mendu DR, Jhang J, Reich D, Sigel K, Cordon-
626 Cardo C, Feldmann M, Parekh S, Merad M, Gnjatic S. 2020. An inflammatory cytokine
627 signature predicts COVID-19 severity and survival. Nat Med 26:1636-1643.
628 36. Diamond MS, Kanneganti TD. 2022. Innate immunity: the first line of defense against
629 SARS-CoV-2. Nat Immunol 23:165-176.
630 37. Stanifer ML, Guo C, Doldan P, Boulant S. 2020. Importance of Type I and III
631 Interferons at Respiratory and Intestinal Barrier Surfaces. Front Immunol 11:608645.

632 38. Galani IE, Triantafyllia V, Eleminiadou EE, Koltsida O, Stavropoulos A, Manioudaki M,
633 Thanos D, Doyle SE, Kotenko SV, Thanopoulou K, Andreakos E. 2017. Interferon-
634 lambda Mediates Non-redundant Front-Line Antiviral Protection against Influenza
635 Virus Infection without Compromising Host Fitness. Immunity 46:875-890 e6.
636 39. Lokugamage KG, Hage A, de Vries M, Valero-Jimenez AM, Schindewolf C, Dittmann
637 M, Rajsbaum R, Menachery VD. 2020. Type I interferon susceptibility distinguishes
638 SARS-CoV-2 from SARS-CoV. bioRxiv doi:10.1101/2020.03.07.982264.
639 40. Vanderheiden A, Ralfs P, Chirkova T, Upadhyay AA, Zimmerman MG, Bedoya S,
640 Aoued H, Tharp GM, Pellegrini KL, Manfredi C, Sorscher E, Mainou B, Lobby JL,
641 Kohlmeier JE, Lowen AC, Shi PY, Menachery VD, Anderson LJ, Grakoui A, Bosinger
642 SE, Suthar MS. 2020. Type I and Type III Interferons Restrict SARS-CoV-2 Infection
643 of Human Airway Epithelial Cultures. J Virol 94.
644 41. Cameron MJ, Ran L, Xu L, Danesh A, Bermejo-Martin JF, Cameron CM, Muller MP,
645 Gold WL, Richardson SE, Poutanen SM, Willey BM, DeVries ME, Fang Y, Seneviratne
646 C, Bosinger SE, Persad D, Wilkinson P, Greller LD, Somogyi R, Humar A, Keshavjee
647 S, Louie M, Loeb MB, Brunton J, McGeer AJ, Canadian SRN, Kelvin DJ. 2007.
648 Interferon-mediated immunopathological events are associated with atypical innate
649 and adaptive immune responses in patients with severe acute respiratory syndrome.
650 J Virol 81:8692-706.
651 42. Wang S, Li W, Hui H, Tiwari SK, Zhang Q, Croker BA, Rawlings S, Smith D, Carlin
652 AF, Rana TM. 2020. Cholesterol 25-Hydroxylase inhibits SARS-CoV-2 and other
653 coronaviruses by depleting membrane cholesterol. EMBO J 39:e106057.
654 43. Zang R, Case JB, Yutuc E, Ma X, Shen S, Gomez Castro MF, Liu Z, Zeng Q, Zhao H,
655 Son J, Rothlauf PW, Kreutzberger AJB, Hou G, Zhang H, Bose S, Wang X, Vahey
656 MD, Mani K, Griffiths WJ, Kirchhausen T, Fremont DH, Guo H, Diwan A, Wang Y,
657 Diamond MS, Whelan SPJ, Ding S. 2020. Cholesterol 25-hydroxylase suppresses
658 SARS-CoV-2 replication by blocking membrane fusion. Proc Natl Acad Sci U S A
659 117:32105-32113.
660 44. Hauser AS, Chavali S, Masuho I, Jahn LJ, Martemyanov KA, Gloriam DE, Babu MM.
661 2018. Pharmacogenomics of GPCR Drug Targets. Cell 172:41-54 e19.
662 45. Sinha S, Cheng K, Schaffer AA, Aldape K, Schiff E, Ruppin E. 2020. In vitro and in
663 vivo identification of clinically approved drugs that modify ACE2 expression. Mol Syst
664 Biol 16:e9628.
665 46. Saheb Sharif-Askari N, Saheb Sharif-Askari F, Alabed M, Tayoun AA, Loney T, Uddin
666 M, Senok A, Al Heialy S, Hamoudi R, Kashour T, Alsheikh-Ali A, Hamid Q, Halwani R.
667 2020. Effect of Common Medications on the Expression of SARS-CoV-2 Entry
668 Receptors in Kidney Tissue. Clin Transl Sci 13:1048-1054.
669 47. Li J, Liao X, Zhou Y, Wang L, Yang H, Zhang W, Zhang Z, Kang Y. 2021. Association
670 between glucocorticoids treatment and viral clearance delay in patients with COVID-
671 19: a systematic review and meta-analysis. BMC Infect Dis 21:1063.
672 48. Gandhi S, Klein J, Robertson AJ, Pena-Hernandez MA, Lin MJ, Roychoudhury P, Lu
673 P, Fournier J, Ferguson D, Mohamed Bakhash SAK, Catherine Muenker M,
674 Srivathsan A, Wunder EA, Jr., Kerantzas N, Wang W, Lindenbach B, Pyle A, Wilen
675 CB, Ogbuagu O, Greninger AL, Iwasaki A, Schulz WL, Ko AI. 2022. De novo
676 emergence of a remdesivir resistance mutation during treatment of persistent SARS-
677 CoV-2 infection in an immunocompromised patient: a case report. Nat Commun
678 13:1547.
679 49. Wallis RS, O'Garra A, Sher A, Wack A. 2022. Host-directed immunotherapy of viral
680 and bacterial infections: past, present and future. Nat Rev Immunol
681 doi:10.1038/s41577-022-00734-z.

682

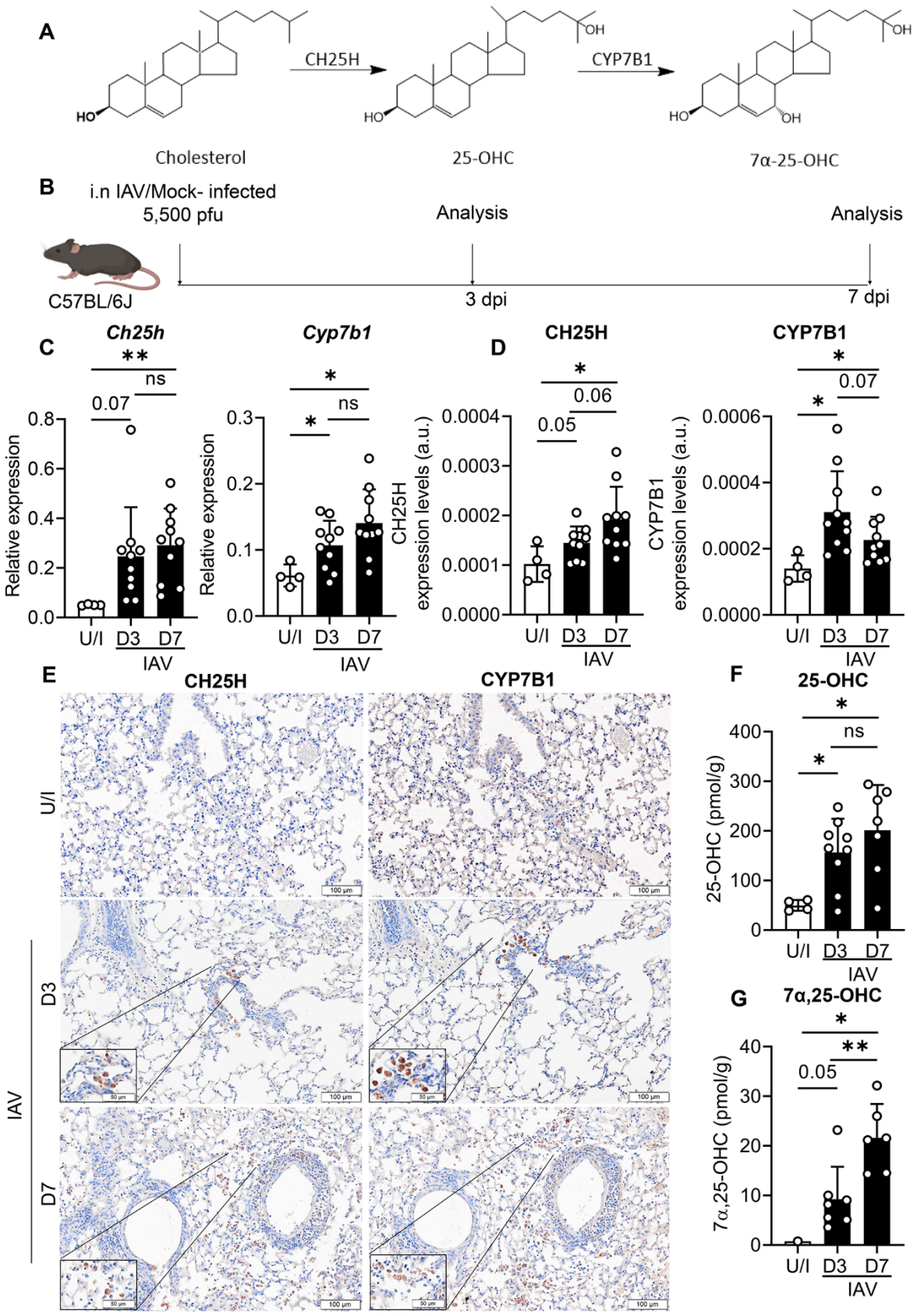
A
CH25H
CYP7B1
HO
OH
Cholesterol
25-OHC
7α-25-OHC
B
i.n IAV/Mock- infected
5,500 pfu
Analysis
Analysis
C57BL/6J
3 dpi
7 dpi
C
Ch25h
Cyp7b1
Relative expression
U/I
D3
D7
IAV
D
CH25H
CYP7B1
CH25H expression levels (a.u.)
CYP7B1 expression levels (a.u.)
E
CH25H
CYP7B1
U/I
D3
D7
IAV
F
25-OHC
25-OHC (pmol/g)
G
7α,25-OHC
7α,25-OHC (pmol/g)

683

684 **Figure 1. IAV infection leads to upregulation of CH25H and CYP7B1 expression in the**
685 **lung and production of the oxysterols 25-OHC and 7α,25-OHC**

686 **A**) The biosynthetic pathway of 25-OHC and 7α,25-OHC. **B**) Experimental design. C57BL/6J
687 mice were infected intranasally with 5,500 PFU of A/Auckland/01/09 and mRNA expression
688 of **C**) *Ch25h* and *Cyp7b1* were measured by qRT-PCR at 3 dpi and 7 dpi normalized to *Hprt*.
689 **D**) Quantitative analysis of CH25H and CYP7B1 protein labelling by IHC. **E**) Representative
690 IHC images of CH25H and CYP7B1 in lung sections of uninfected or IAV-infected mice.
691 Concentrations of **F**) 25-OHC and **G**) 7α,25-OHC in the lungs at 3 dpi and 7 dpi expressed
692 in pmol per gram lung tissue. Data are presented as mean ± SD of n=4 uninfected and n=6-
693 10 infected mice per timepoint. Scale Bar = 100μm; dpi = days post-infection; U/I = mock
694 infected; ns., not significant; *, $P < 0.05$; **, $P < 0.01$ indicate significant differences.

695

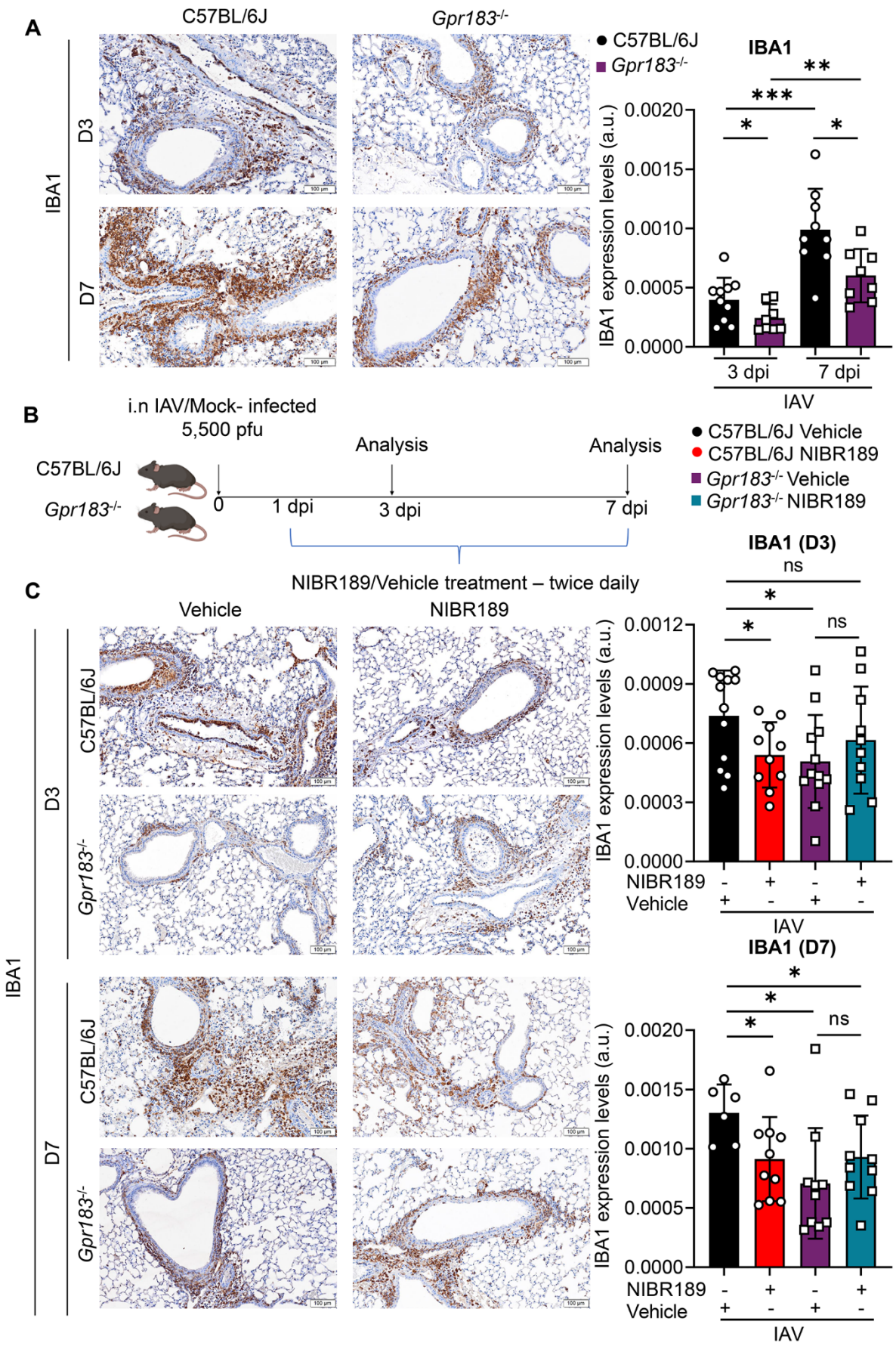
A
C57BL/6J
Gpr183-/-
IBA1
D3
D7
C57BL/6J
Gpr183-/-
IBA1
IBA1 expression levels (a.u.)
0.0020
0.0015
0.0010
0.0005
0.0000
3 dpi
7 dpi
IAV
B
i.n IAV/Mock- infected
5,500 pfu
C57BL/6J
Gpr183-/-
0
1 dpi
Analysis
3 dpi
Analysis
7 dpi
NIBR189/Vehicle treatment – twice daily
C57BL/6J Vehicle
C57BL/6J NIBR189
Gpr183-/- Vehicle
Gpr183-/- NIBR189
C
Vehicle
NIBR189
IBA1 (D3)
IBA1 (D7)
ns
NIBR189
Vehicle
IAV

696

697 **Figure 2. Deletion of the *Gpr183* gene or administration of a GPR183 antagonist**
698 **reduces macrophage infiltration in IAV-infected lungs.** C57BL/6J and *Gpr183*$^{-/-}$ mice
699 were infected intranasally with 5,500 PFU of A/Auckland/01/09. **A**) Representative IHC
700 images of IBA1 in lung sections of IAV-infected C57BL/6J and *Gpr183*$^{-/-}$ mice. Quantitative
701 analysis of IBA1 staining. **B**) Experimental design; C57BL/6J mice and *Gpr183*$^{-/-}$ mice were
702 infected intranasally with 5,500 PFU of A/Auckland/01/09. Mice were subsequently treated
703 orally with 7.6 mg/kg NIBR189 or vehicle control twice daily from 1 dpi until the end of the
704 experiment. **C**) Representative IHC images of IBA1 in lung sections of C57BL/6J and *Gpr183*$^{-}$
705 $^{/-}$ mice with the respective treatment groups at 3dpi and 7dpi. Quantitative analysis of IBA1
706 staining. Data are presented as mean ± SD of n = 6-12 infected mice per genotype and
707 timepoint. dpi = days post-infection; Scale Bar = 100µm; U/I = mock infected ns = not
708 significant; *, $P < 0.05$; **, $P < 0.01$; ***, $P < 0.001$ indicate significant differences

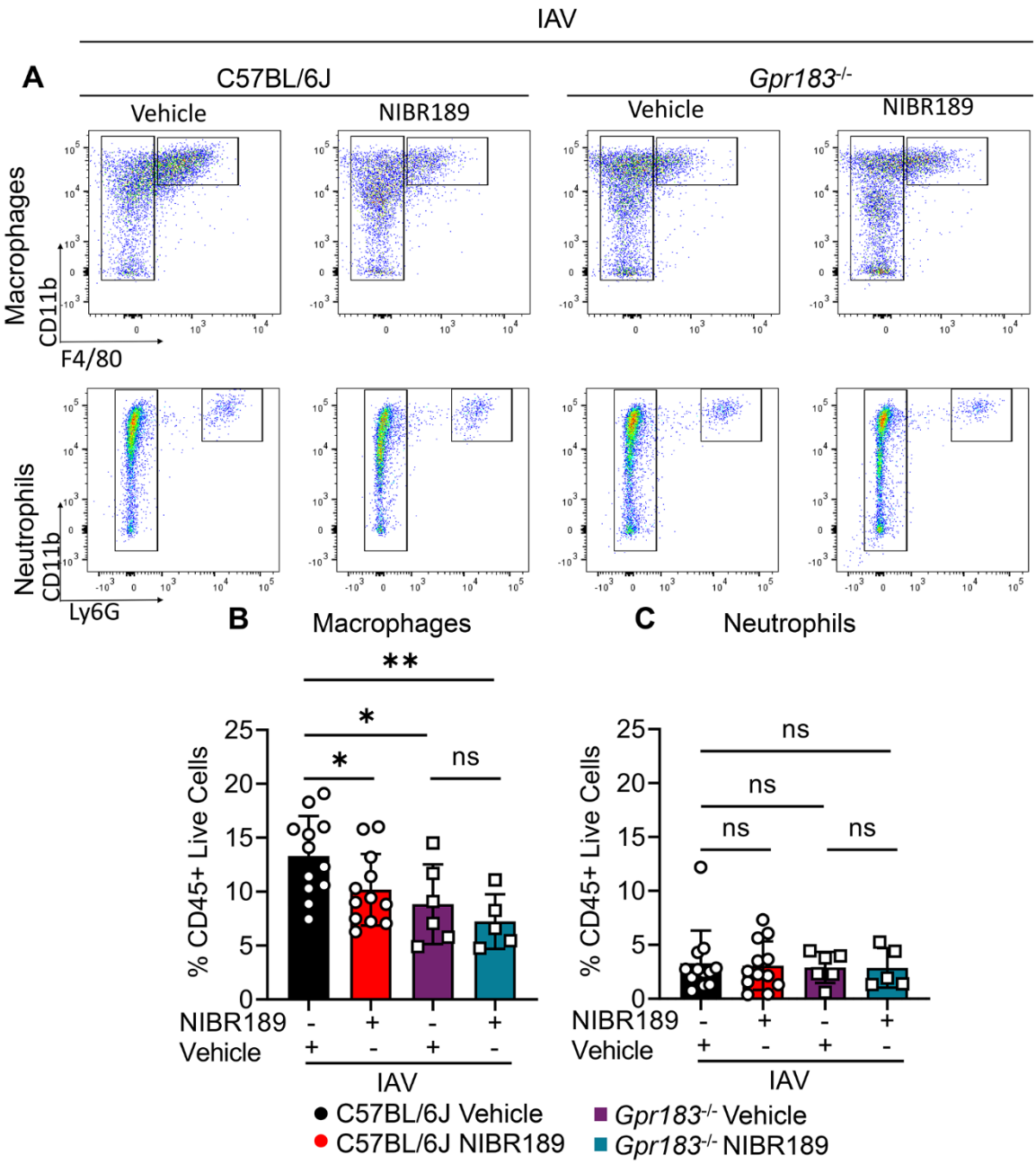

Figure 3. The GPR183 antagonist NIBR189 reduces macrophage infiltration and inflammatory cytokine production. C57BL/6J and *Gpr183*$^{-/-}$ mice were infected intranasally with 5,500 PFU of A/Auckland/01/09. Mice were subsequently treated orally with 7.6 mg/kg NIBR189 or vehicle control twice daily from 1 dpi until the end of the experiment. **A**) Frequency of infiltrating macrophages (F480^{high}/CD11b^{+}/Ly6G^{-}/SigF^{-}) and neutrophils (B220^{-} CD3^{-}Ly6G^{+}) was determined by flow cytometry relative to total viable CD45^{+} immune cells 3 dpi. Graphs depicting the frequency of **B**) macrophages and **C**) neutrophils. Data are presented as mean ± SD of n=5-12 infected mice per genotype and timepoint. dpi = days

718 post-infection; U/I = mock infected; ns = not significant; *, $P < 0.05$; **, P<0.01 indicate
719 significant differences.

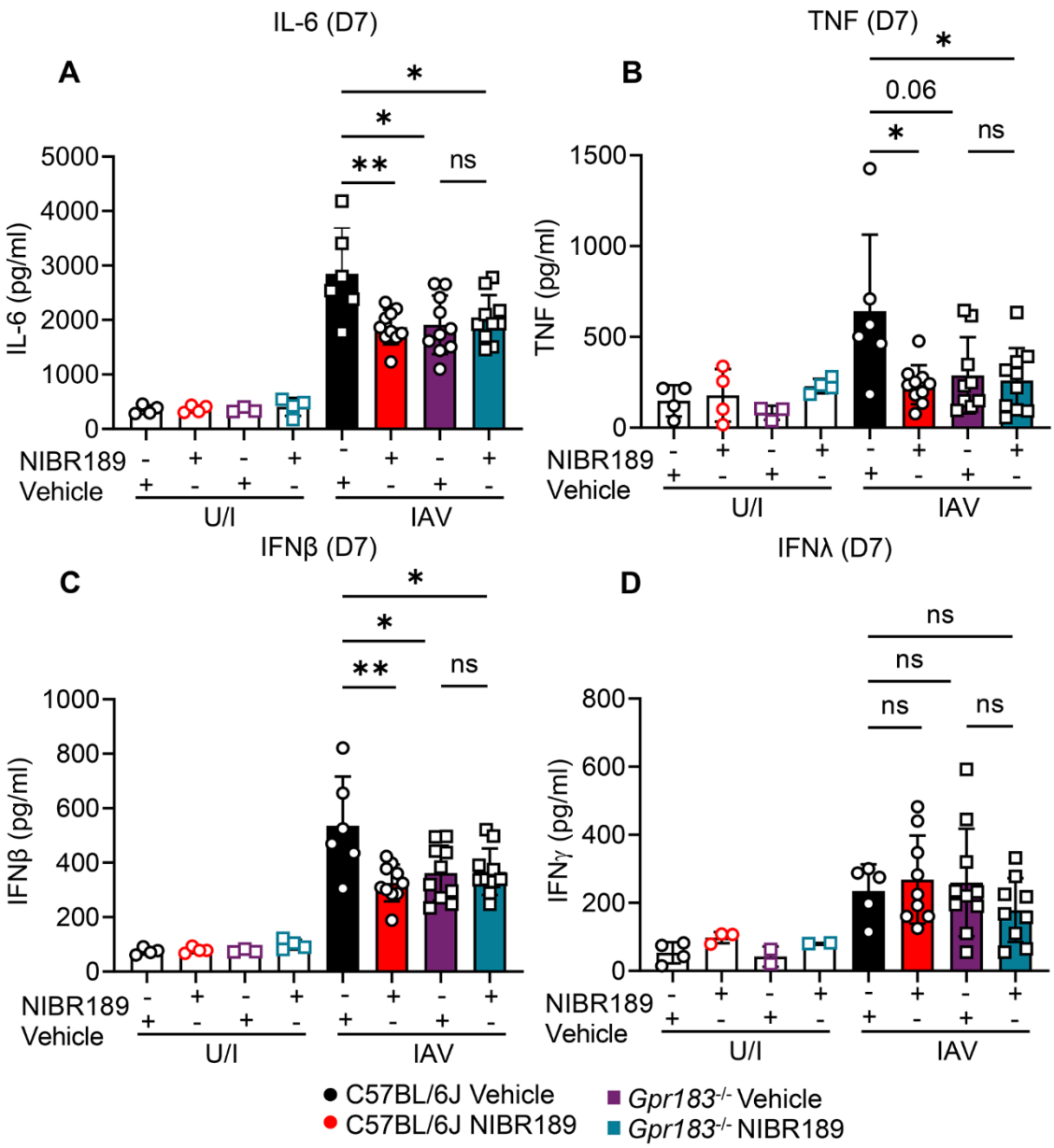

720

721 **Figure 4. The GPR183 antagonist NIBR189 reduces inflammatory cytokine production.**
722 C57BL/6J and *Gpr183*$^{-/-}$ mice were infected intranasally with 5,500 PFU of A/Auckland/01/09.
723 Mice were subsequently treated orally with 7.6 mg/kg NIBR189 or vehicle control twice daily
724 from 1 dpi until the end of the experiment. Cytokine measurements of **A**) IL-6, **B**) TNF, **C**)
725 IFNβ and **D**) IFNλ at 7 dpi measured by ELISA. Data are presented as mean ± SD of n=5-12
726 infected mice per genotype and timepoint. dpi = days post-infection; U/I = mock infected; ns
727 = not significant; *, $P < 0.05$; **, P<0.01 indicate significant differences.

728

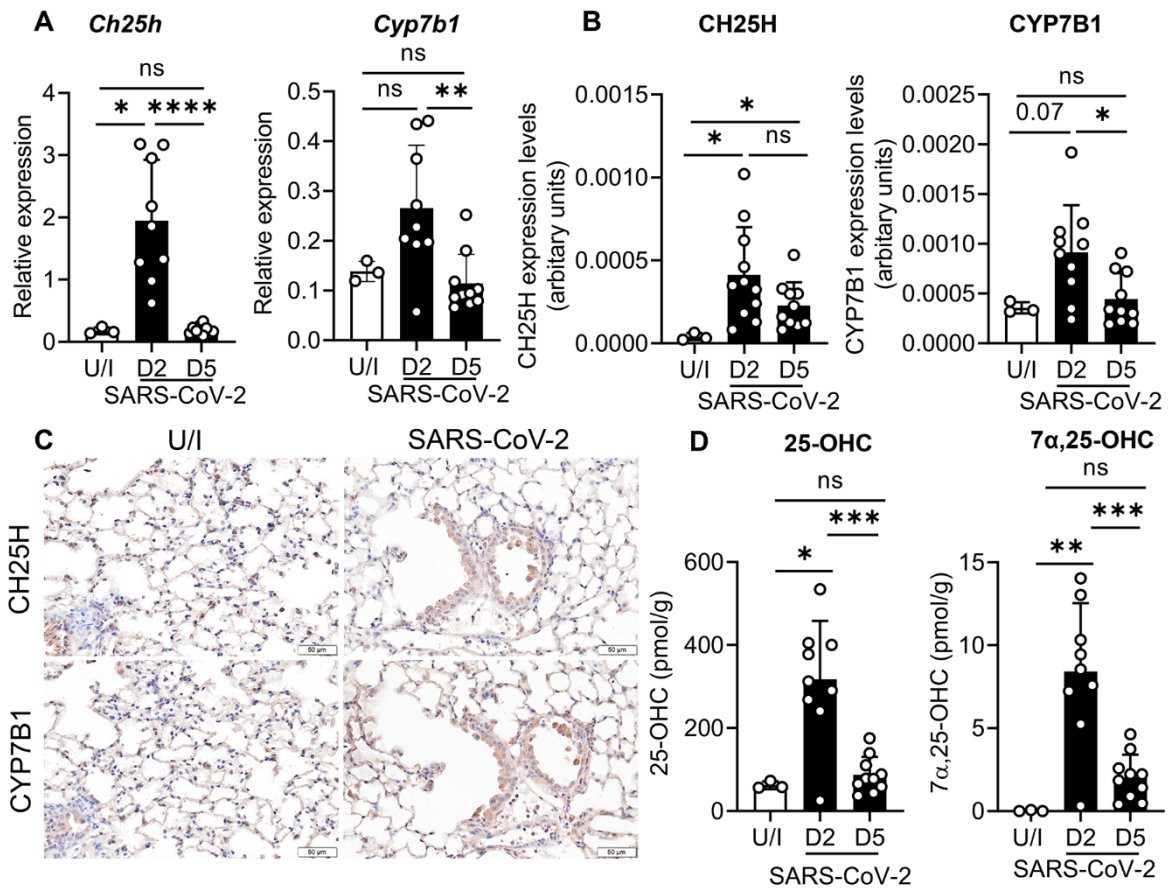

Figure 5. SARS-CoV-2 infection leads to upregulation of CH25H and CYP7B1 expression in the lung and production of the oxysterols 25-OHC and 7α,25-OHC. C57BL/6J mice were infected intranasally with approximately 8x10^4 PFU of mouse-adapted SARS-CoV-2. mRNA expression of **A**) *Ch25h* and *Cyp7b1* was measured by qRT-PCR at 2 dpi and 5 dpi normalized to *Hprt*. **B**) Quantitative analysis of CH25H and CYP7B1 protein by IHC labelling and **C**) representative IHC images of CH25H and CYP7B1 in lung sections in uninfected, 2 dpi and 5 dpi. **D**) Concentrations of 25-OHC and 7α,25-OHC in the lungs at 2 dpi and 5 dpi expressed in pmol per gram lung tissue. Data are presented mean ± SD of n=3 uninfected mice and n= 9-10 infected mice per timepoint. Scale Bar = 50μm; U/I = mock infected; dpi = days post-infection; ns = not significant; *, $P < 0.05$; **, $P < 0.01$; ***, $P < 0.001$; ****, $P < 0.0001$ indicate significant differences.

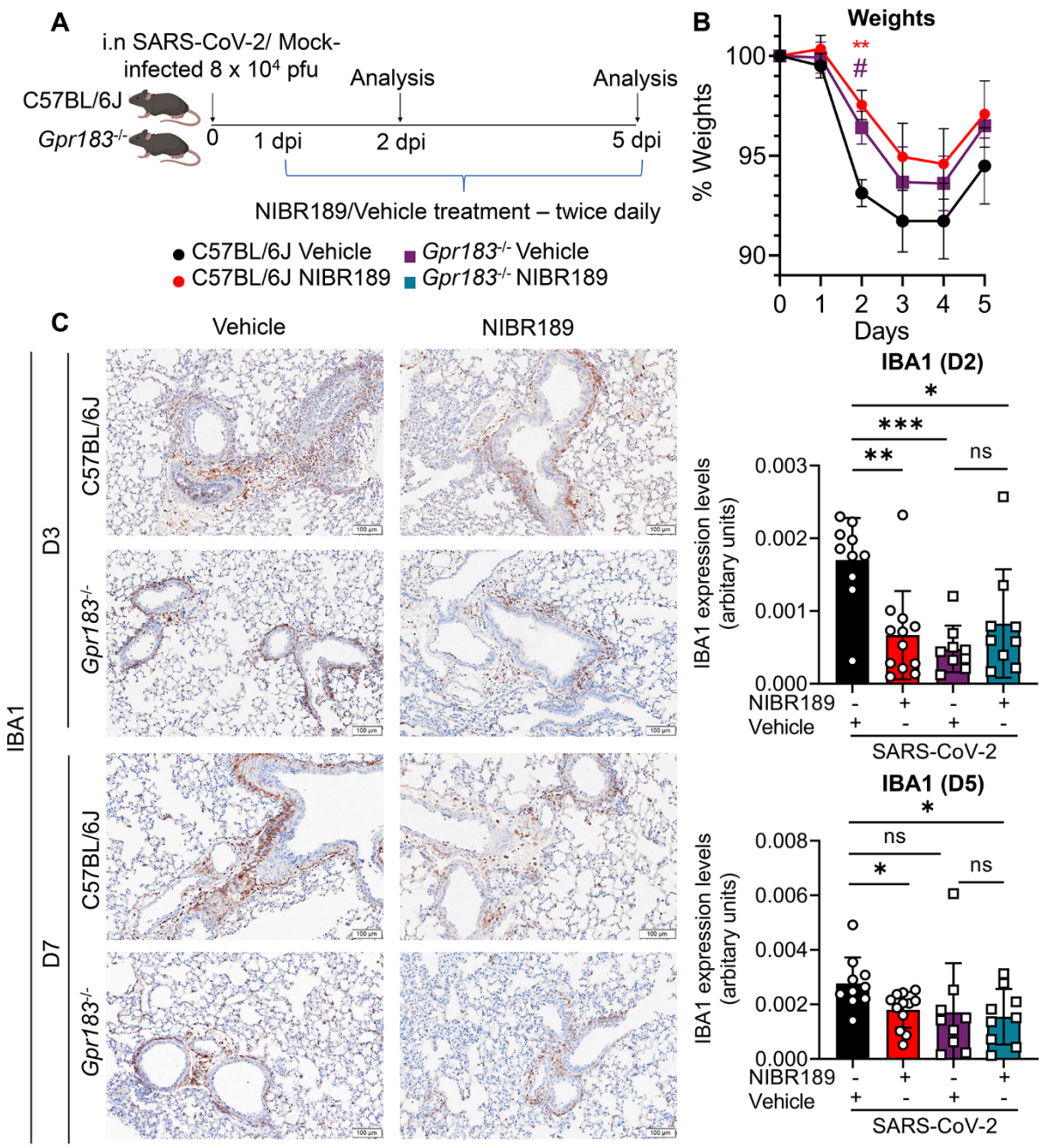

Figure 6. GPR183 inhibition resulted in less SARS-CoV-2 infection-induced weight loss and in reduced macrophage infiltration. C57BL/6J and *Gpr183*$^{-/-}$ mice were infected intranasally with approximately 8x10^4 PFU of mouse-adapted SARS-CoV-2. Mice were subsequently treated orally with 7.6 mg/kg NIBR189 or vehicle control twice daily from 1 dpi until the end of the experiment. **A**) Experimental design. **B**) Weights of mice displayed as percentage of the weight at time of inoculation. **C**) Representative IHC images of IBA1 in lung of C57BL/6J and *Gpr183*$^{-/-}$ mice with the respective treatment groups at 2 dpi and 5 dpi (left). Scale Bar = 100µm. Quantitative analysis of IBA1 (right). Data are presented mean ± SD of n=9-12 infected mice per genotype and timepoint. Scale Bar = 100µm; U/I uninfected; dpi =

752 days post-infection; ns = not significant; *, $P < 0.05$; **, $P < 0.01$; ***, $P < 0.001$ indicate
753 significant differences.

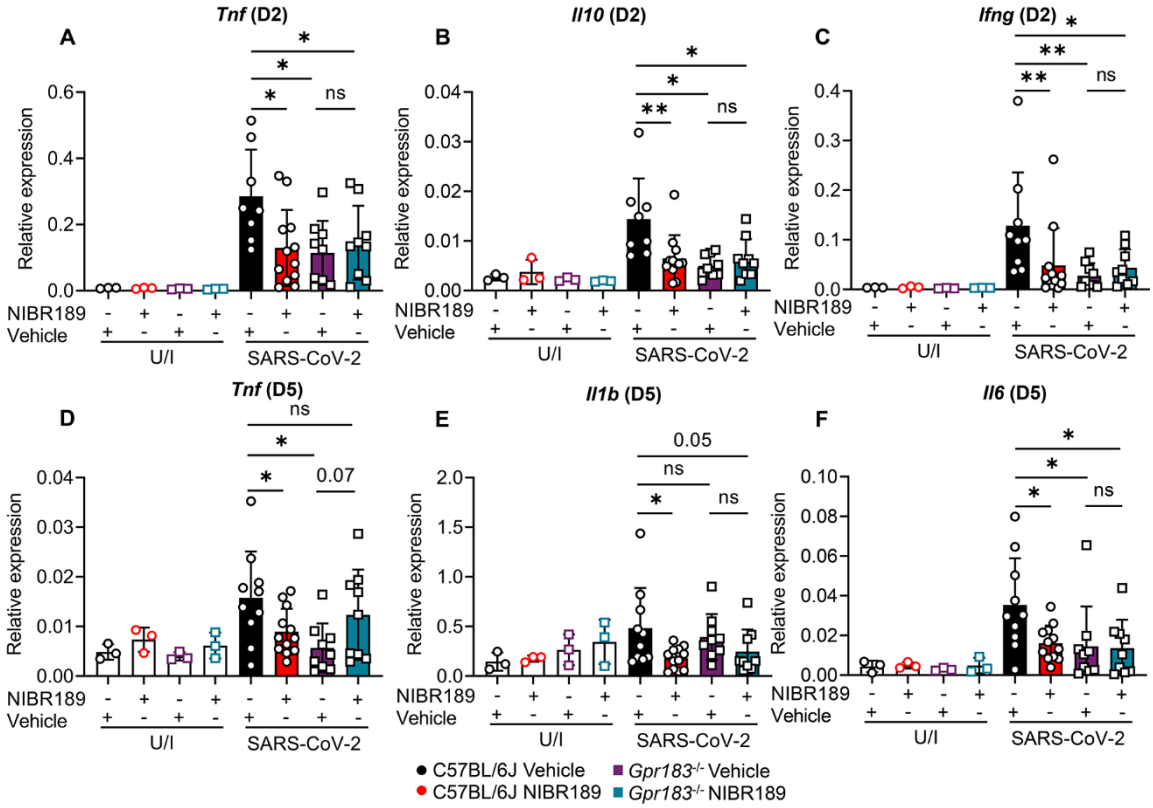

754

755 **Figure 7. GPR183 inhibition led to reduced inflammatory cytokine profile.** C57BL/6J
756 and *Gpr183*$^{-/-}$ mice were infected intranasally with approximately 8x10^4 PFU of mouse-
757 adapted SARS-CoV-2. Mice were subsequently treated orally with 7.6 mg/kg NIBR189 or
758 vehicle control twice daily from 1 dpi until the end of the experiment. Relative expression of
759 **A**) *Tnf*, **B**) *Il10*, **C**) *Ifng* at 2 dpi and **D**) *Tnf*, **E**) *Il1b*, **F**) *Il6* at 5 dpi in the lungs measured by
760 RT-qPCR, normalized to *Hprt*. Data are presented mean ± SD of n=3 uninfected mice and
761 n= 9-12 infected mice per genotype and timepoint. U/I = mock infected; dpi = days post-
762 infection; ns = not significant; *, $P < 0.05$; **, $P < 0.01$; ***, $P < 0.001$ indicate significant
763 differences.

764

765

766

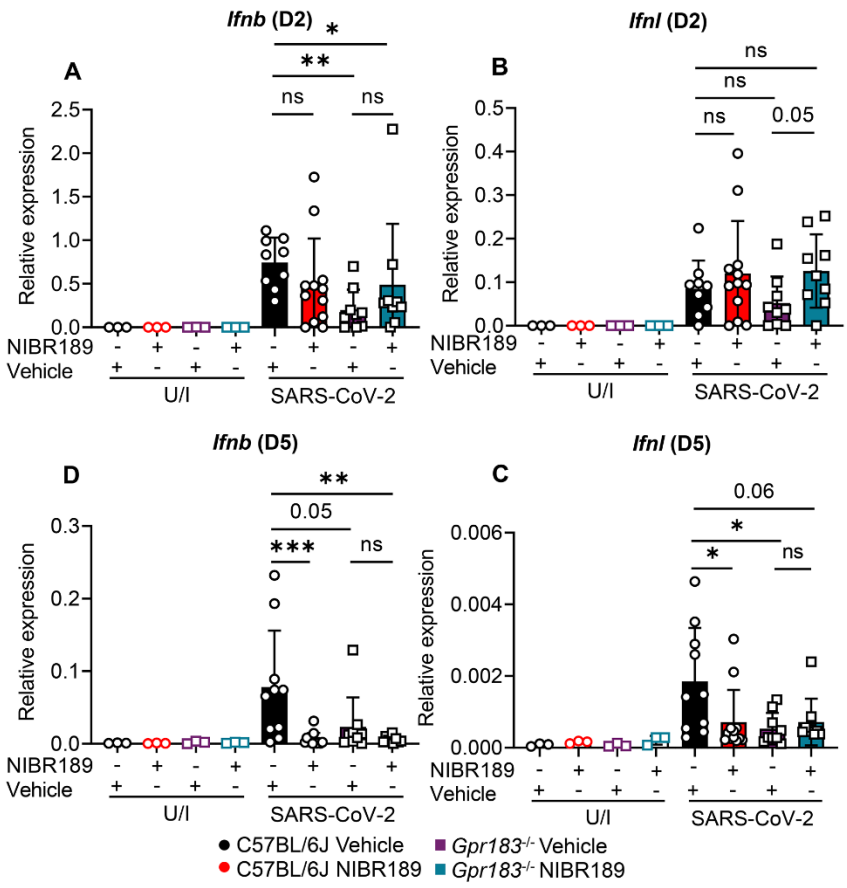

Figure 8. GPR183 inhibition led to reduced interferon responses at 5 dpi. C57BL/6J and *Gpr183*$^{-/-}$ mice were infected intranasally with approximately 8x10^4 PFU of mouse-adapted SARS-CoV-2. Mice were subsequently treated orally with 7.6 mg/kg NIBR189 or vehicle control twice daily from 1 dpi until the end of the experiment. Relative expression of **A**) *Ifnb*, **B**) *Ifnl* at 2 dpi and **C**) *Ifnb*, **D**) *Ifnl* at 5 dpi in the lungs measured by RT-qPCR, normalized to *Hprt*. Data are presented mean ± SD of n=3 uninfected mice and n= 9-12 infected mice per genotype and timepoint. U/I = mock infected; dpi = days post-infection; ns = not significant; *, $P < 0.05$; **, $P < 0.01$; ***, $P < 0.001$ indicate significant differences.

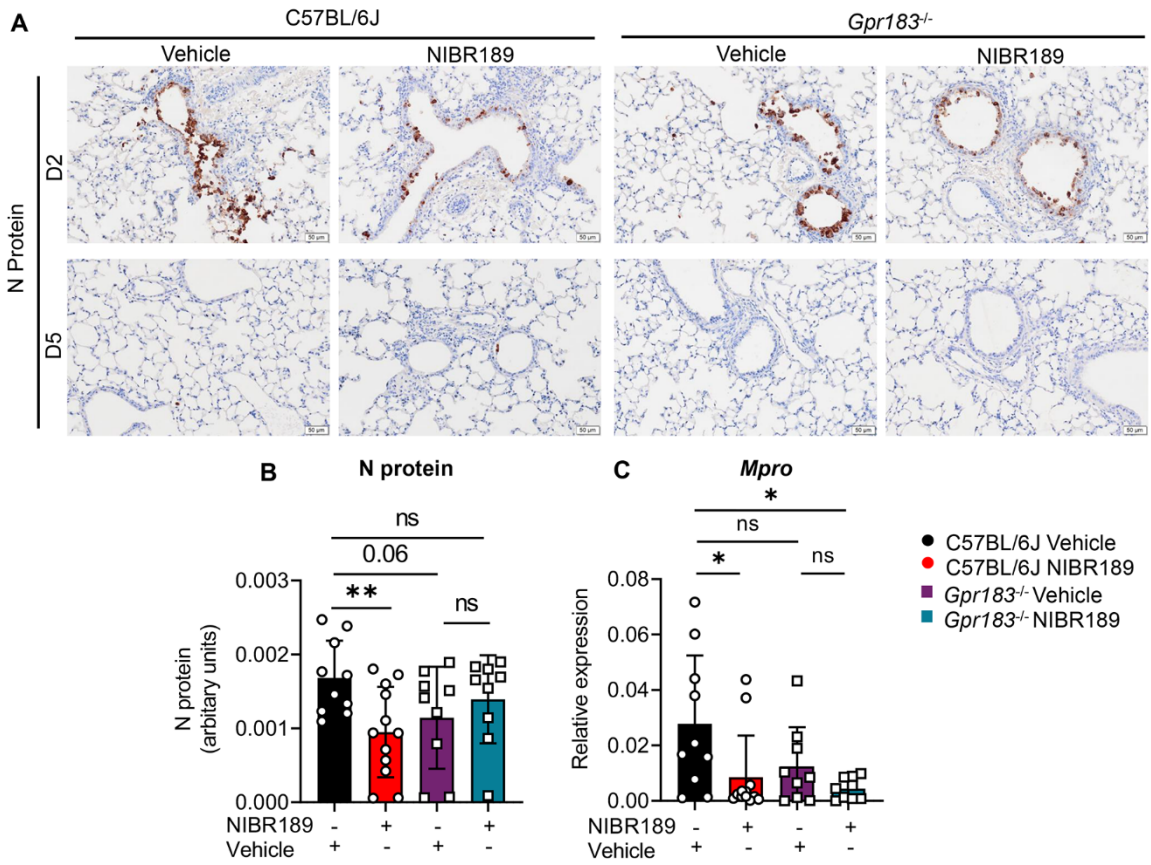

Figure 9. Mice treated with GPR183 antagonist had lower SARS-CoV-2 loads.

C57BL/6J and *Gpr183*$^{-/-}$ mice were infected intranasally with approximately 8x10^4 PFU of mouse-adapted SARS-CoV-2. Mice were subsequently treated orally with 7.6 mg/kg NIBR189 or vehicle control twice daily from 1 dpi until the end of the experiment. **A**) Representative IHC images of viral nucleocapsid (Np) expression at 2 dpi and 5dpi. **B**) Quantitative analysis of viral Np expression of the treatment groups at 2 dpi. **C**) Viral load was assessed in the lung through the detection of *Mpro* RNA by RT-qPCR at 5 dpi, normalized to HPRT. Data are presented mean ± SD of n=9-12 infected mice per genotype and timepoint. Scale Bar = 50µm; U/I = mock infected; dpi = days post-infection; ns = not significant; *, $P < 0.05$; **, $P < 0.01$, indicate significant differences.

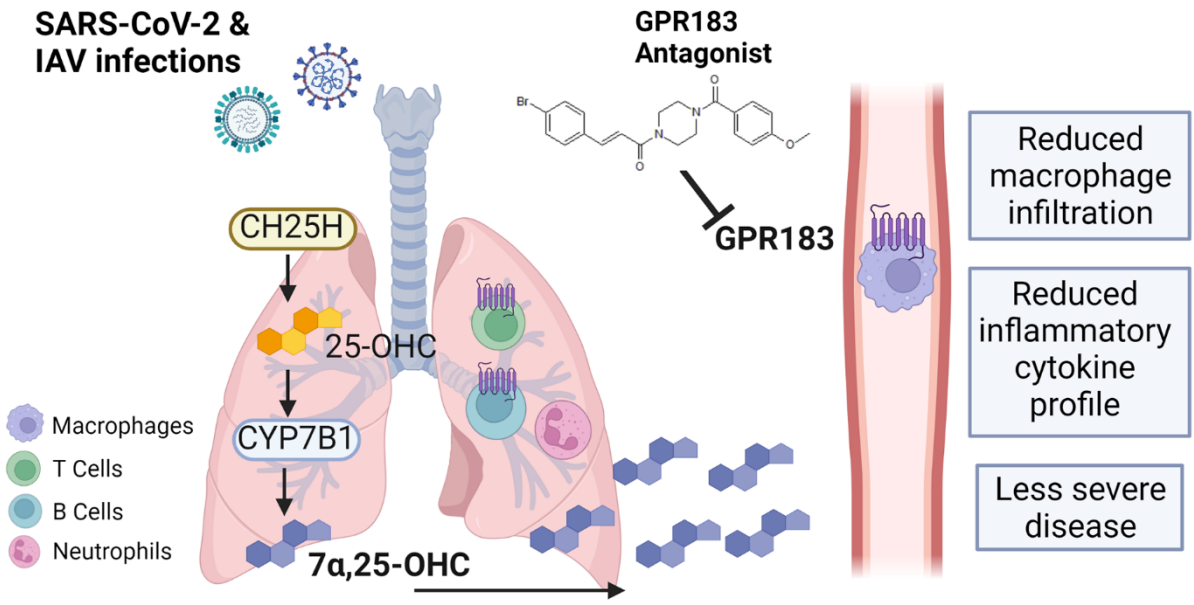

Figure 10. Schematic figure of the role of GPR183 in the immune response to SARS-CoV-2 and IAV infections. SARS-CoV-2 and IAV infections lead to the upregulation of CH25H and CYP7B1 which results in the production of 7α,25-OHC. This oxysterol chemotactically attracts GPR183-expressing macrophages to the lungs where they produce pro-inflammatory cytokines. Pharmacological inhibition of GPR183 attenuates the infiltration of GPR183-expressing macrophages, leading to reduced production of inflammatory cytokines without negatively affecting antiviral responses.

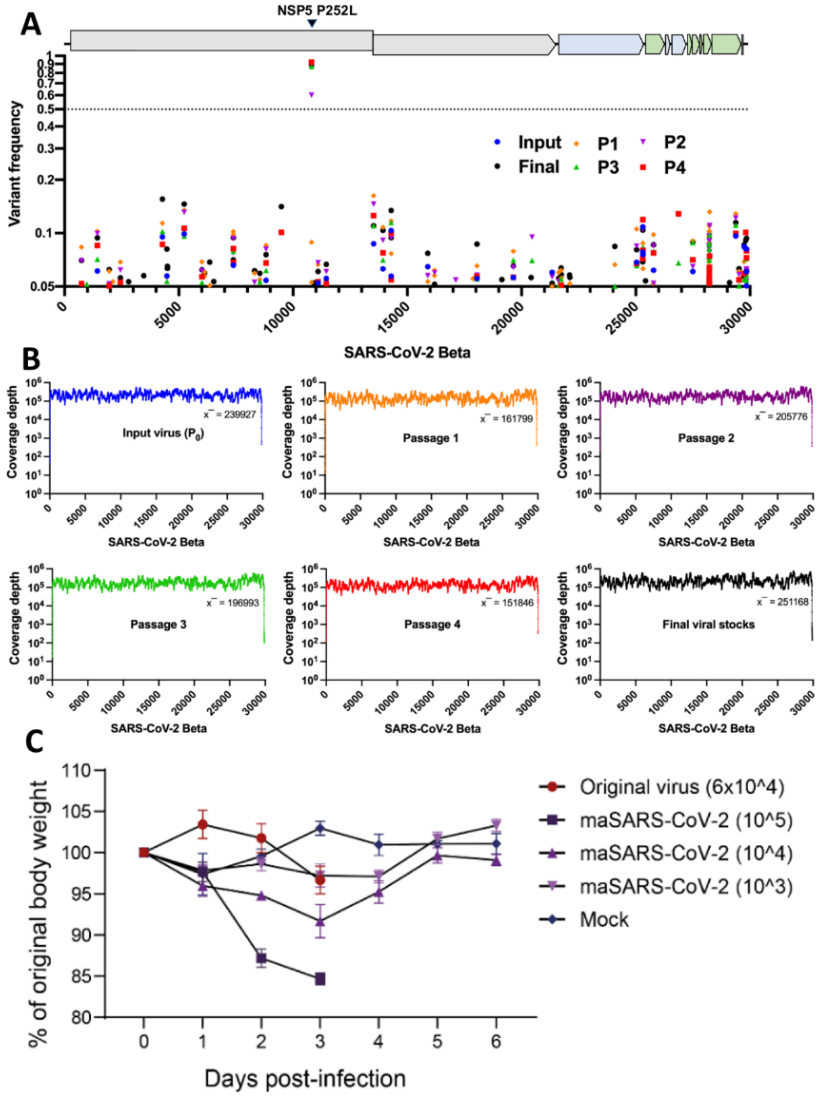

807

808 **Figure S1. Evolution and coverage of mouse-adapted SARS-CoV-2 virus. A**) Mutation
809 frequency of input SARS-CoV-2 Beta virus (blue circle) and passage one (orange diamond),
810 passage two (purple nabla), passage three (green triangle) and passage four (red square)
811 mouse-adapted viruses over the reference genome sequence as well as the final virus stocks
812 (black circle) amplified in VeroE6-hTMPRSS2 cells. The dotted line indicates the consensus
813 frequency of 0.5 **B**) Summary plots of read coverage of passaged SARS-CoV-2 viruses from
814 A) mapping to SARS-CoV-2 Beta strain. Depth of coverage of binary alignment files was
815 determined using samtools depth. **C**) Weight loss over time following infection with the Beta
816 variant of SARS-CoV-2 (original virus) or various doses of maSARS-CoV-2 (after four
817 passages in mice). Plaque forming units are indicated in brackets. Data indicates mean ±
818 SEM.

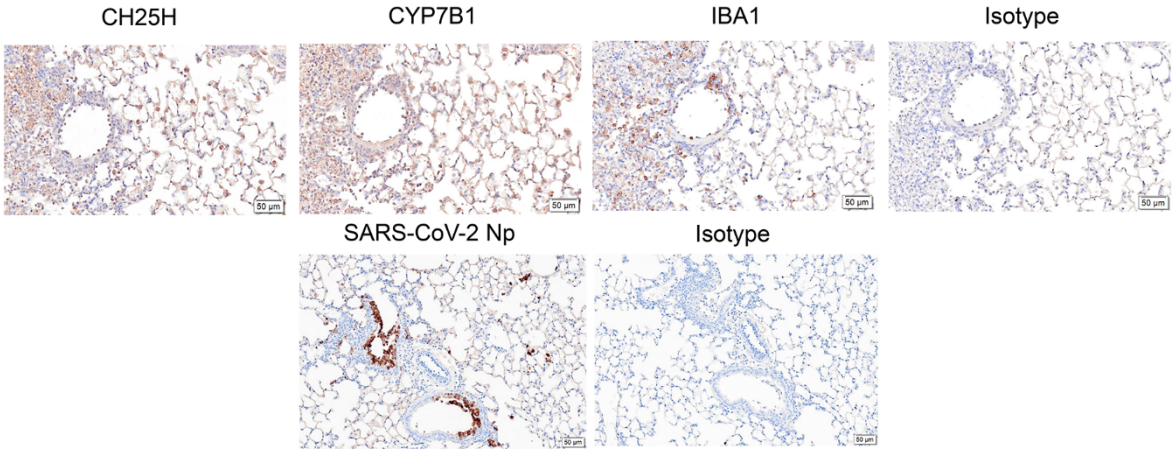

Figure S2. Isotype staining controls for CYP7B1, CH25H, IBA1 and viral Np. IHC of IAV-infected lung sections incubated with rabbit anti-CH25H, rabbit anti-CYP7B, rabbit anti-IBA1 and an isotype-matched control (Rabbit IgG; negative control). IHC of SARS-CoV-2-infected lung sections incubated with rabbit anti-SARS-CoV-2 nucleocapsid protein (Np) and an isotype-matched control (Rabbit IgG; negative control). Scale bar = 50µm

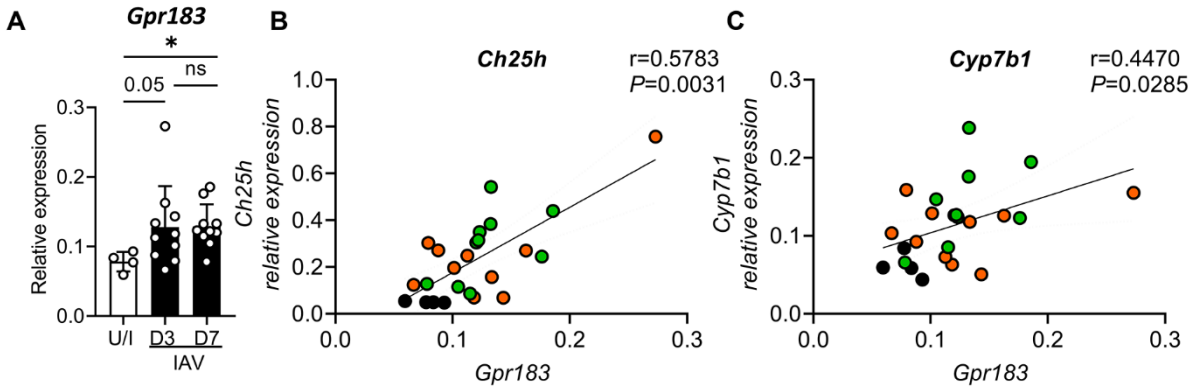

Figure S3. *Gpr183* mRNA expression is upregulated in the lung during IAV infection and correlates with expression of the oxysterol synthesising enzymes CH25H and CYP7B1. C57BL/6J mice were infected intranasally with 5,500 PFU of A/Auckland/01/09. **A**) Relative expression of *Gpr183* mRNA measured by RT-qPCR, normalized to *Hprt*. Correlation analyses were performed with mRNA expression levels of *Gpr183* and oxysterol synthesizing enzymes. Individual scatter plots showing correlations between *Gpr183* and **B**) *Ch25h* and **C**) *Cyp7b1*. Black dots represent uninfected samples while coloured dots represent IAV-infected samples (Orange dots, 3 dpi; green dots, 7 dpi). Data are presented as mean ± SD of n=4 uninfected and n=8-10 infected mice per timepoint. ns = not significant; *, $P < 0.05$ indicate significant differences. Spearman rank correlation test were used to

837 calculate correlation coefficient and to determine significant correlations with values
838 displayed on each scatter plot.

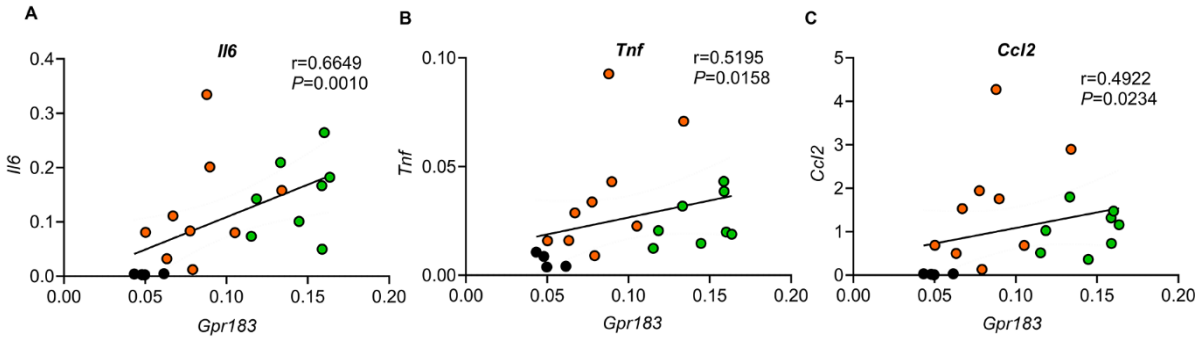

839

840 **Figure S4. Correlations between lung mRNA expression of *Gpr183* and inflammatory**
841 **markers in IAV-infected mice.**

842 Correlation analyses of *Gpr183* mRNA expression with mRNA expression of inflammatory
843 cytokines in lung tissue from IAV-infected C57BL/6J mice (n=21 pairs). Relative gene
844 expression was determined by RT-qPCR, normalized to *Hprt*. Individual scatter plots showing
845 correlations between *Gpr183* and **A**) *Il6*, **B**) *Tnf* and **C**) *Ccl2*. Black dots represent uninfected
846 samples while coloured dots represent IAV-infected samples (Orange dots, 3dpi; green dots,
847 7dpi). Spearman rank correlation test were used to calculate correlation coefficient and to
848 determine significant correlations with values displayed on each scatter plot.

849

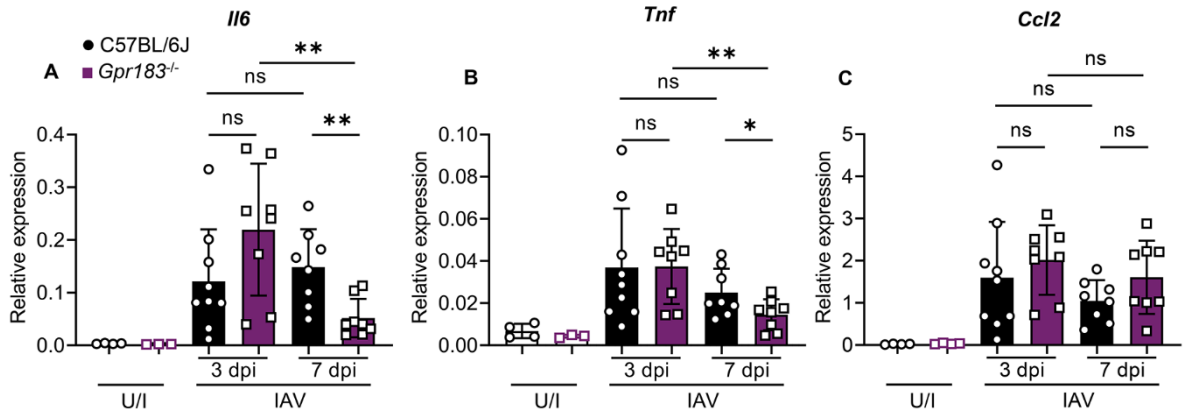

850

851 **Figure S5. Cytokine expression at mRNA and protein level in IAV-infected C57BL/6J**
852 **and *Gpr183*$^{-/-}$ mice.** C57BL/6J and *Gpr183*$^{-/-}$ mice were infected intranasally with 5,500 PFU
853 of A/Auckland/01/09. Cytokine measurements of **A**) *Il6,* **B**) *Tnf* and **C**) *Ccl2* at 3 dpi and 7 dpi
854 measured by RT-qPCR, normalized to *Hprt.* Data are presented as mean ± SD of n=4

855 uninfected per genotype and n=8-10 infected mice per genotype and timepoint. U/I =
856 uninfected; dpi = days post-infection; ns = not significant; *, $P < 0.05$; **, $P < 0.01$ indicate
857 significant differences.

858

859

860

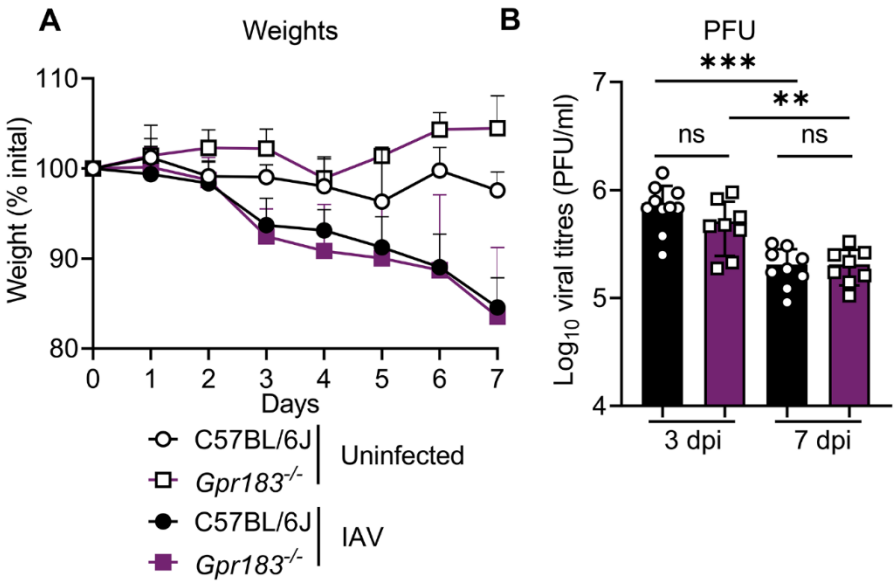

861

862 **Figure S6. Weights of IAV and mock infected C57BL/6J and *Gpr183*$^{-/-}$ mice and viral**
863 **loads.** C57BL/6J and *Gpr183*$^{-/-}$ mice were infected intranasally with approximately 5,500 PFU
864 of A/Auckland/01/09. **A**) Weights of IAV- or mock-inoculated mice are displayed as
865 percentage of the weight at time of inoculation. **B**) Viral load was assessed by measuring the
866 PFU by plaque assays. Data are presented as mean ± SD for n=8-10 infected mice per
867 genotype and timepoint. dpi = days post-infection; ns = not significant; **, $P < 0.01$; ***, $P <$
868 0.001 indicate significant differences.

869

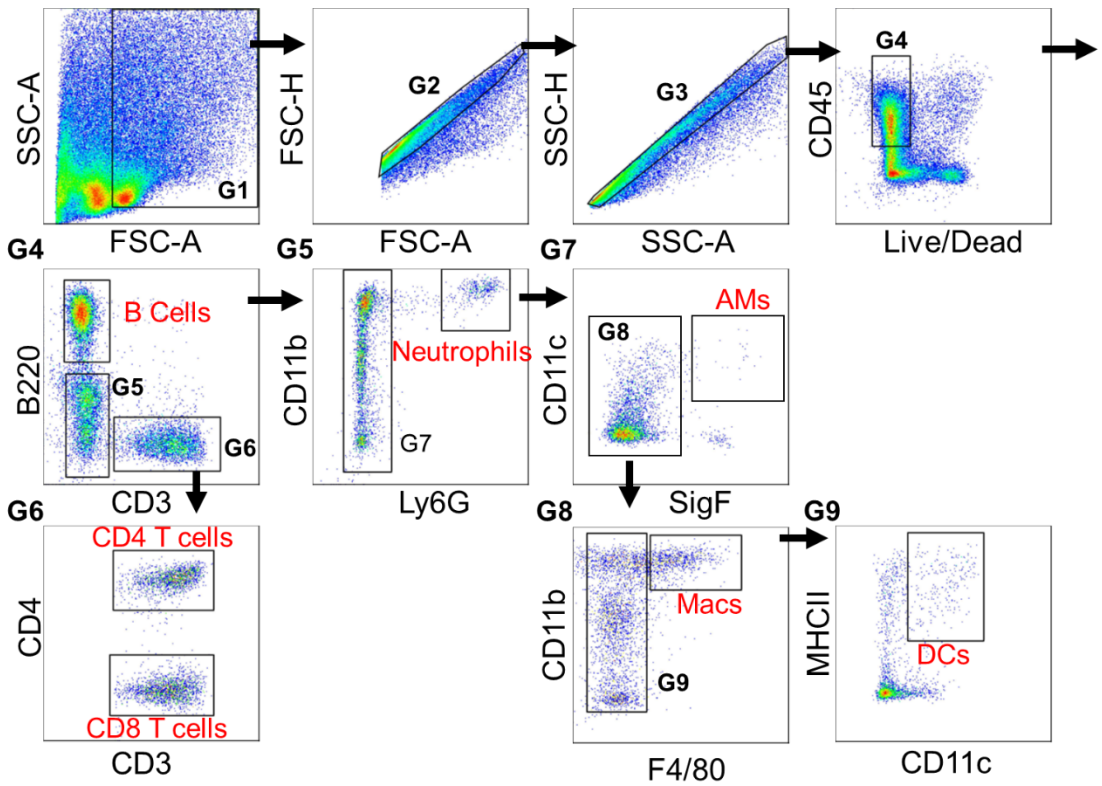

870

871 **Figure S7. Representative flow cytometry plots illustrating the gating strategy of**
872 **immune cells.** C57BL/6J or *Gpr183*$^{-/-}$ mice were infected intranasally with 5,500 PFU of
873 A/Auckland/01/09. Mice were subsequently treated orally with 7.6 mg/kg NIBR189 or vehicle
874 control twice daily from 1 dpi until the end of the experiment. Gates containing multiple cell
875 populations are numbered (G1-G9). Gates that contained a single cell population are labeled
876 with its respective cell type. These includes: B cells (B220^{+}; G5), CD4^{+} T cells (CD3^{+},CD4^{+};
877 G6), CD8^{+} T Cells (CD3^{+},CD4^{-}; G6), Neutrophils (B220^{-},CD3^{-},Ly6G^{+}; G5), Alveolar
878 macrophages (B220^{-},CD3^{-},Ly6G^{-},CD11c^{+},SigF^{+}; G7), Macrophages (B220^{-},CD3^{-},Ly6G^{-}
879 ,SigF^{-},CD11b^{+},F4/80^{high}; G8) and Dendritic cells (DCs; B220^{-},CD3^{-},Ly6G^{-},SigF^{-},
880 F4/80^{low},CD11c^{+}, MHCII^{+}; G9).

881

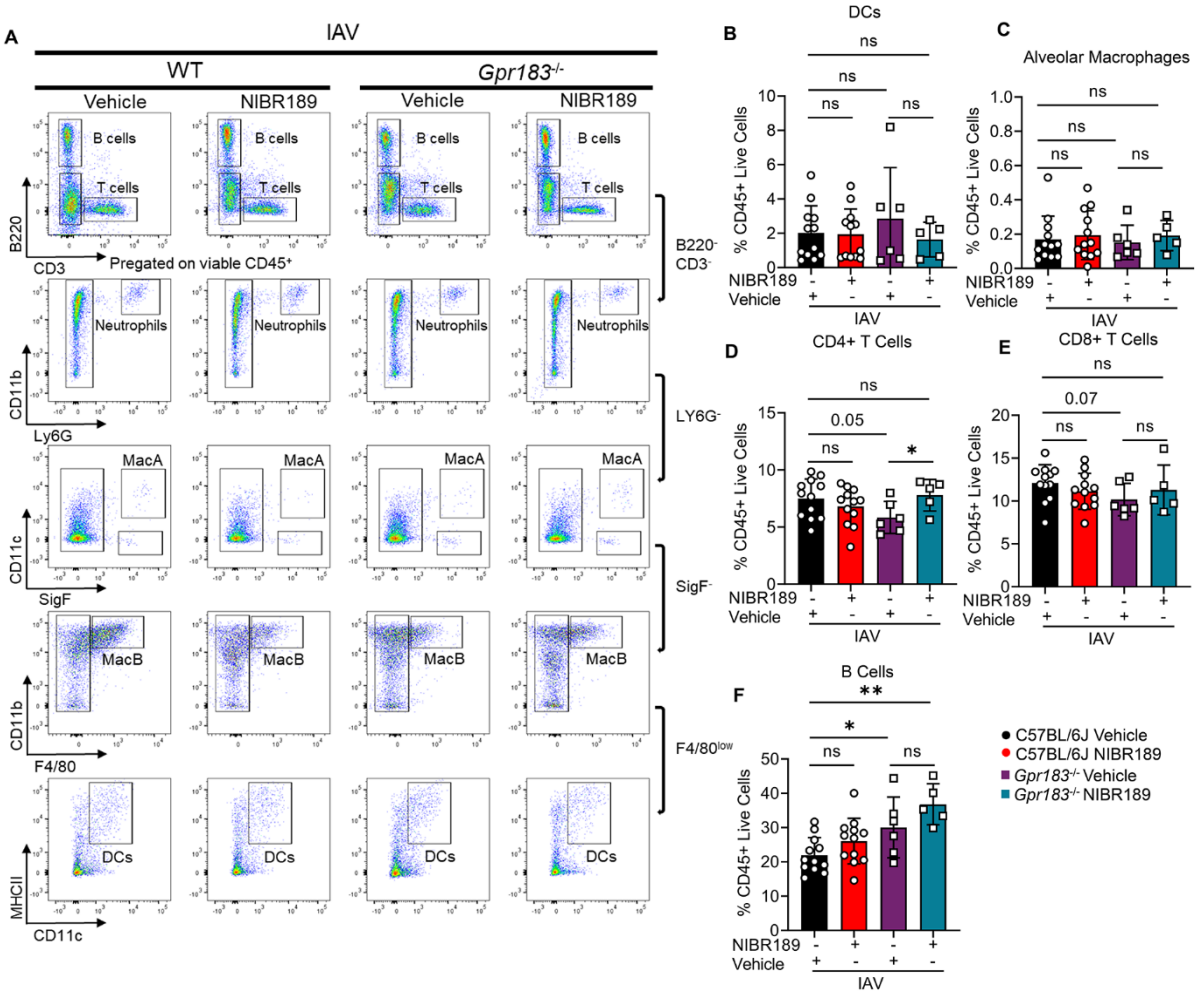

Figure S8. Immune cell populations in the lungs of IAV-infected mice treated with the GPR183 antagonist NIBR189. C57BL/6J or *Gpr183*$^{-/-}$ mice were infected intranasally with 5,500 PFU of A/Auckland/01/09. Mice were subsequently treated orally with 7.6 mg/kg NIBR189 or vehicle control twice daily from 1 dpi until the end of the experiment. **A**) Frequency of B cells (B220^{+}), T cells (CD3^{+} CD8^{+} or CD4^{+}), neutrophils (B220^{-}CD3^{-}Ly6G^{+}) was determined by flow cytometry against total viable CD45^{+} immune cells at 3 dpi. Alveolar macrophages (CD11c^{+}SigF^{+}), infiltrating macrophages (F480^{high}/CD11b^{+}/Ly6G^{-}/SigF^{-}) and dendritic cells (SigF^{-}F4/80^{-}MHCII^{+}CD11c^{+}) were further identified from the B220^{-}CD3^{-}Ly6G^{-} cell population. (**B-G**) Graphs depicting the frequency of **B**) Dendritic cells, **C**) alveolar macrophages, **D**) CD4^{+} T cells, **E**) CD8^{+} T cells and **F**) B cells against total viable CD45^{+} immune cells. Data are presented mean ± SD of n=5-12 infected mice per genotype and timepoint. UI = uninfected; dpi = days post-infection; ns = not significant.

897

898

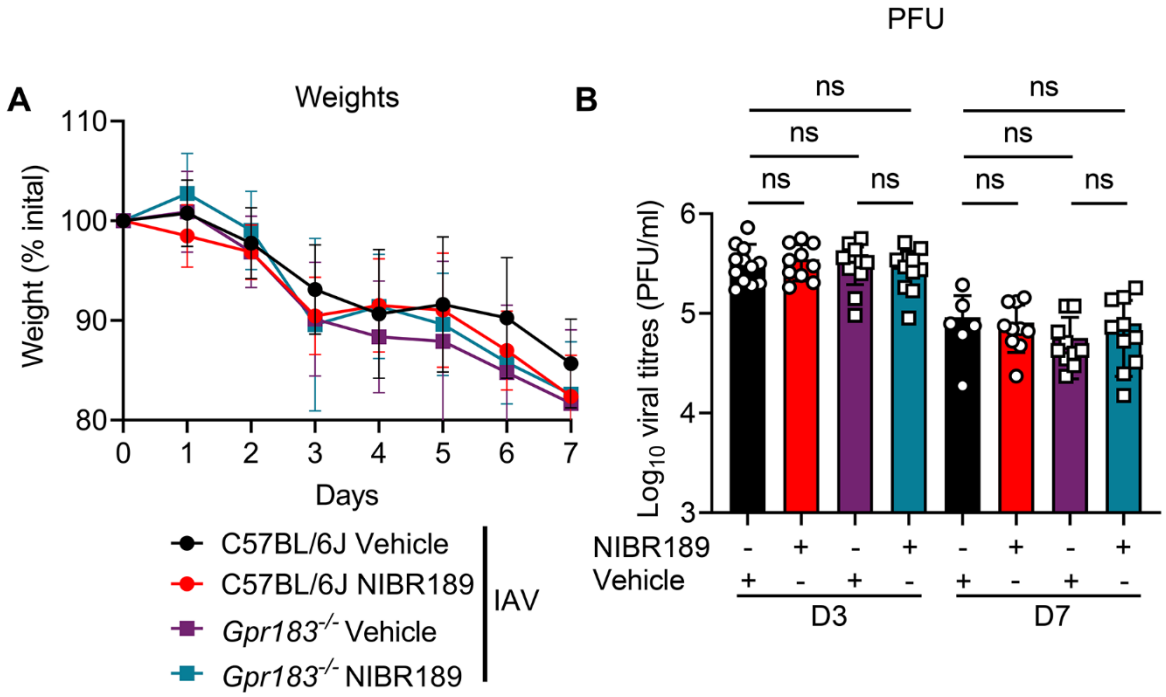

899

900 **Figure S9. Body weights and viral loads of IAV-infected C57BL/6J and *Gpr183*$^{-/-}$ mice**
901 **treated with NIBR189 or vehicle.** C57BL/6J mice and *Gpr183*$^{-/-}$ mice were infected
902 intranasally with 5,500 PFU of A/Auckland/01/09. Mice were subsequently treated orally with
903 7.6 mg/kg NIBR189 or vehicle control twice daily from 1 dpi until the end of the experiment.
904 **A**) Weights of IAV- or mock-inoculated mice with or without treatment are displayed as
905 percentage of the weight at time of inoculation. **B**) Viral load was assessed by measuring the
906 PFU through plaque assay. Data are presented mean ± SD of n=6-12 infected mice per
907 genotype and timepoint. UI = uninfected; dpi = days post-infection; ns = not significant.

908

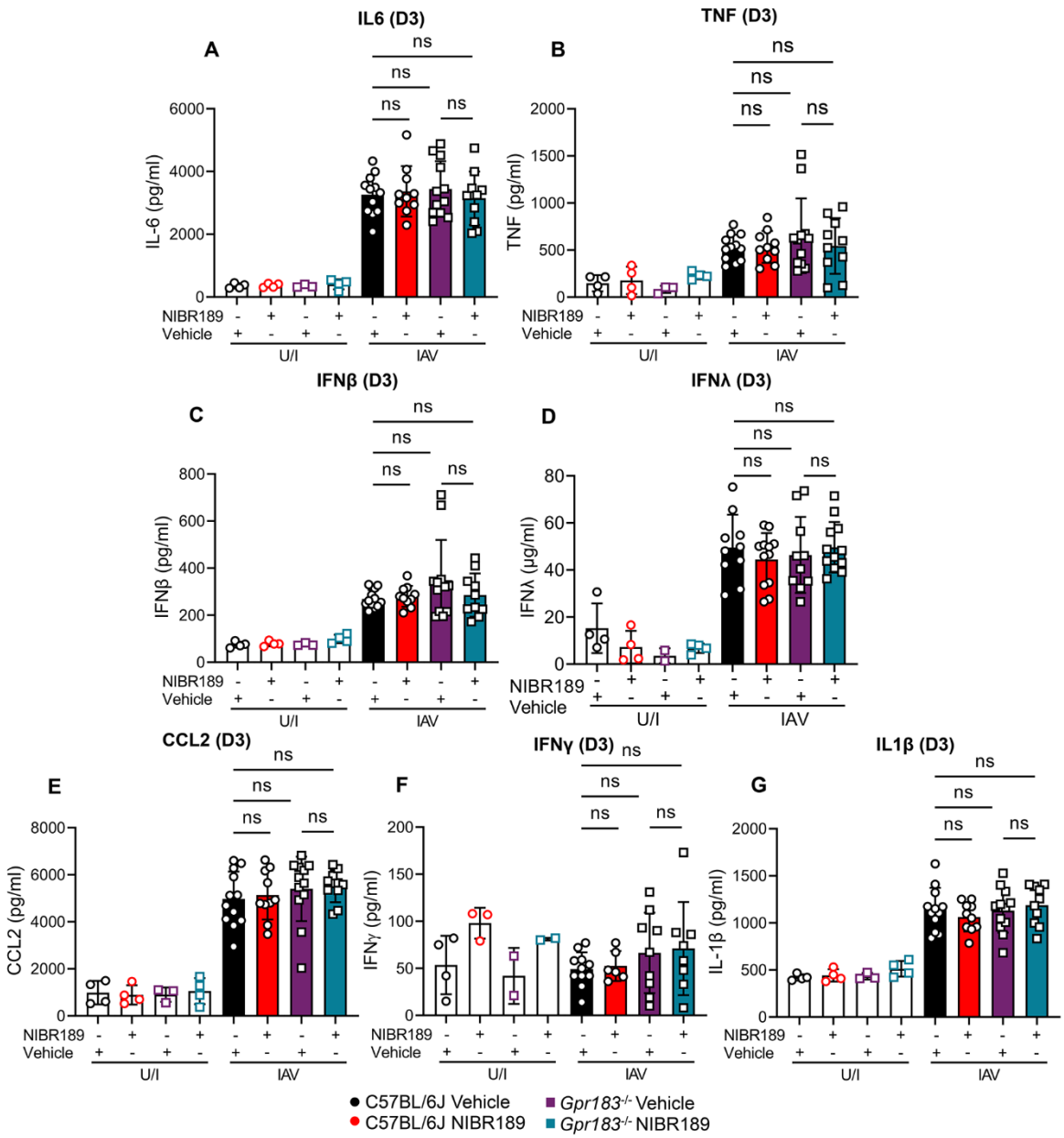

Figure S10. Cytokine expression at protein level in IAV-infected C57BL/6J and *Gpr183*$^{-/-}$ mice treated with NIBR189 and/or vehicle. C57BL/6J and *Gpr183*$^{-/-}$ mice were infected intranasally with 5,500 PFU of A/Auckland/01/09. Mice were subsequently treated orally with 7.6 mg/kg NIBR189 or vehicle control twice daily from 1 dpi until the end of the experiment. Cytokine measurements of **A**) IL-6 **B**) TNF, **C**) IFNβ, **D**) IFN*λ*, **E**) CCL2, **F**) IFNγ and **G**) IL-1β, at 3 dpi measured by ELISA. Data are presented mean ± SD of n=4 uninfected mice per genotype and n=6-12 infected mice per genotype. U/I = uninfected; dpi = days post-infection; ns = not significant. *, $P < 0.05$ indicate significant differences.

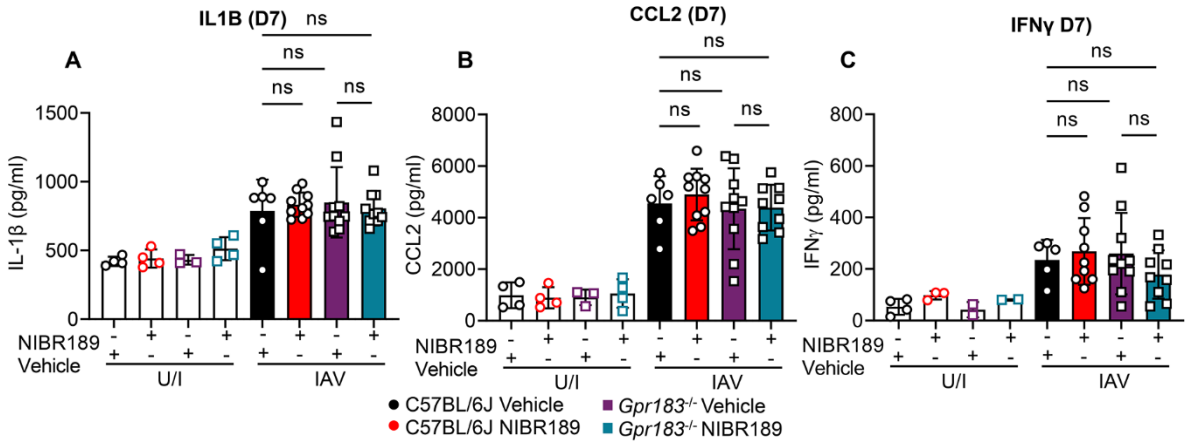

Figure S11. Cytokine expression at protein level in IAV-infected C57BL/6J and *Gpr183*$^{-/-}$ mice treated with NIBR189 and/or vehicle. C57BL/6J and *Gpr183*$^{-/-}$ mice were infected intranasally with 5,500 PFU of A/Auckland/01/09. Mice were subsequently treated orally with 7.6 mg/kg NIBR189 or vehicle control twice daily from 1 dpi until the end of the experiment. Cytokine measurements of **A**) IL-1β, **B**) CCL2, and **C**) IFNγ at 7 dpi measured by ELISA. Data are presented mean ± SD of n=4 uninfected mice per genotype and n=6-12 infected mice per genotype. U/I = uninfected; dpi = days post-infection; ns = not significant.

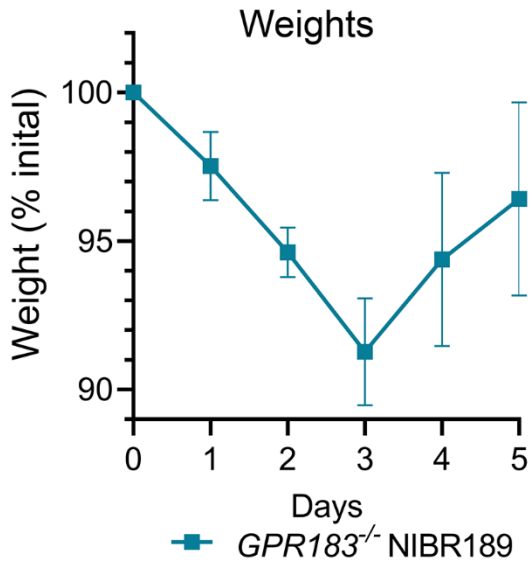

Figure S12. GPR183 inhibition weight loss upon SARS-CoV-2 infection. C57BL/6J and *Gpr183*$^{-/-}$ mice were infected intranasally with approximately 8x10^4 PFU of mouse-adapted SARS-CoV-2. Mice were subsequently treated orally with 7.6 mg/kg NIBR189 or vehicle control twice daily from 1 dpi until the end of the experiment. Weights of mice displayed as percentage of the weight at time of inoculation.

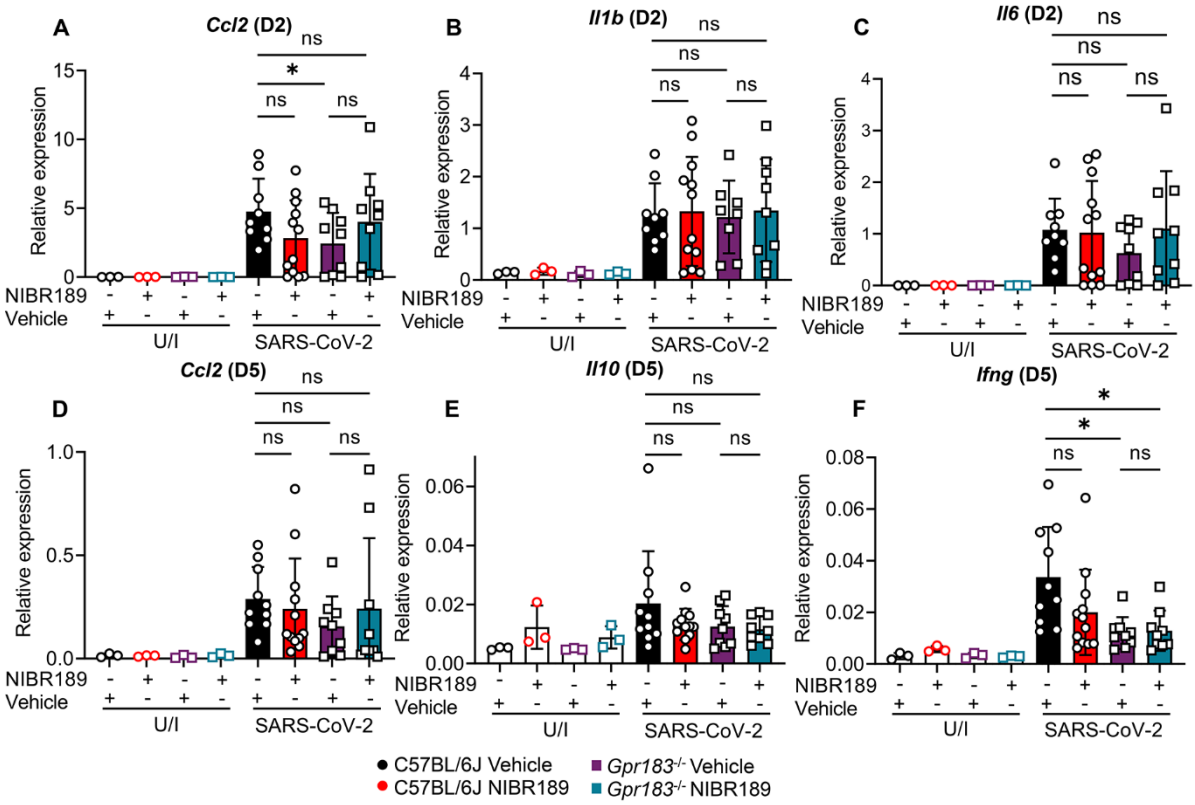

Figure S13. Cytokine expression at mRNA in SARS-CoV-2-infected C57BL/6J and *Gpr183*$^{-/-}$ mice treated with GPR183 antagonist at 2 dpi and 5 dpi. C57BL/6J and *Gpr183*$^{-/-}$ mice were infected intranasally with approximately 8x10^4 PFU of mouse-adapted SARS-CoV-2. Mice were subsequently treated orally with 7.6 mg/kg NIBR189 or vehicle control twice daily from 1 dpi until the end of the experiment. Expression of **A**) *Ccl2*, **B**) *Il1b* and **C**) *Il6* at 2 dpi and **D**) *Ccl2*, **E**) *Il10* and **F**) *Ifng* 5 dpi was measured by RT-qPCR normalized to HPRT. Data are presented mean ± SD of n=3 uninfected mice and n= 9-12 infected; mice per genotype and timepoint. U/I = uninfected dpi = days post-infection; ns = not significant. *, $P < 0.05$; **, $P < 0.01$; ***, $P < 0.001$ indicate significant differences.

950

951

952 **Supplemental Table S1: Primers used in this study**

	Forward	Reverse
Gpr183	GTCGTGTTCATCCTGTGCTTCAC	TCATCAGGCACACCGTGAAGTG
Ch25h	CTGACCTTCTTCGACGTGCT	GGGAAGTCATAGCCCGAGTG
Cyp7b1	CGGAAATCTTCGATGCTCCAAAG	GCTTGTTCCGAGTCCAAAAGGC
Ccl2	GCTACAAGAGGATCACCAGCAG	GTCTGGACCCATTCCTTCTTGG
Hprt1	CCCCAAAATGGTTAAGGTTGC	AACAAAGTCTGGCCTGTATCC
Ifnb1	AACTCCACCAGCAGACAGTG	GGTACCTTTGCACCCTCCAG
Ifng	CAGCAACAGCAAGGCGAAAAAGG	TTTCCGCTTCCTGAGGCTGGAT
Il10	CGGGAAGACAATAACTGCACCC	CGGTTAGCAGTATGTTGTCCAGC
Il1b	TGGACCTTCCAGGATGAGGACA	GTTCATCTCGGAGCCTGTAGTG
Il6	CTGCAAGTGCATCATCGTTGTTC	TACCACTTCACAAGTCGGAGGC
Ifnl	AGCTGCAGGCCTTCAAAAAG	TGGGAGTGAATGTGGCTCAG
Tnf	TAGCCCACGTCGTAGCAAAC	ACAAGGTACAACCCATCGGC
Hif1a	CCTGCACTGAATCAAGAGGTGC	CCATCAGAAGGACTTGCRGGCT
mpro	GAGACAGGTGGTTTCTCAATCG	ACGGCAATTCCAGTTTGAGC

953